

# Cardiac Electrophysiology

## 7.1 Overview

Knowledge concerning the electrophysiology of the heart is necessary for the understanding of many aspects of the physiological and pathophysiological cardiac behavior. The electrophysiology is tightly coupled with the mechanic deformation and the pump function of the heart by controlling the development of tension. Furthermore, various mechano-electrical feedback mechanisms influence the cardiac electrophysiology.

The origin of the electrical activity of the heart are the myocytes, which show like nerve cells an electrical excitability. The electrical excitation of a myocyte is tightly coupled with its mechanical contraction. A propagation of electrical excitation from a myocyte to neighboring myocytes is primarily achieved by intercellular transport of ions via the gap junctions. Additionally, extracellular potentials resulting from the electrical activity of cells or from an external current flow can modulate the propagation and initiate an excitation.

A large amount of experiments was performed to achieve knowledge concerning the cardiac electrophysiology, delivering data of the intra-, extra- and intercellular electrophysiological quantities from specific functional regions and from the heart as an integrated whole. The quantities obtained by the experiments are e.g. voltages across membranes and in the different spatial domains as well as flow and concentrations of ions. The experiments range from the measurement of opening states of single ion channels to the extracorporeal registration of electrograms. The hereby discovered phenomena can be attributed e.g. to changes of the electrophysiological states of cellular components and the intercellular electrical coupling. Relevant components are the cell membrane, its ionic channels, pumps and exchangers, as well as intracellular structures, e.g. the sarcoplasmic reticulum.

The measurement data were partly used to create mathematical models of different levels of abstraction. The models of membrane patches, of single cells and of cell clusters describe the electrophysiological status commonly in a spatially averaged sense by regionally varying concentrations of different

kinds of ions, by the conductivity of ionic channels, and by the activity of ionic pumps and exchangers. The transport of ions through the channels and exchangers is determined from gradients of ionic concentrations and electrical forces. The models allow the simulation of the electrophysiological behavior with numerical methods. A reconstruction of the previously measured data and furthermore the discovery of unknown phenomena can be achieved.

In the following sections different electrophysiological experiments and modeling approaches are described. The description starts with the measuring and modeling approaches of phenomena of cellular components, followed by the whole cell electrophysiological behavior and mechanisms of the intercellular excitation propagation. The description of the electrophysiology of cellular components concerns primarily the phenomena resulting from the behavior of the cell membrane and the sarcoplasmic reticulum.

In this context the classical work of Hodgkin and Huxley is presented, who delivered quantitative data of the electrophysiology of a squid axon and constructed a mathematical model. Most electrophysiological models of nerve and muscle cells base on their mathematical formulation.

Special focus is given to experiments delivering quantitative data and physically motivated models. In addition, mechano-electrical feedback mechanisms are described for the different levels of measurement and modeling.

## 7.2 Cellular Electrophysiology

### 7.2.1 Experimental Studies

**Cell Membrane.** The cell membrane consists of a phospholipid bilayer, which is perforated by pores formed by proteins (Sect. 6.2.1). The membrane suppresses the diffusion of ions and molecules into and out of the cell. The membrane separates the intra- and extracellular space with different ionic concentrations. The gradient of ionic concentrations is resulting from transport mechanisms and the cellular metabolism.

The electrical behavior of a cellular membrane can be measured *in vivo* and *in situ* with two intracellular electrodes. One of the electrodes is used for applying current and one for the registration of the transmembrane voltage. A third electrode is located in the extracellular space near to the cell. The measurement procedure is relatively insensitive with regard to the placement of the electrodes, resulting from the high resistivity of the membrane in contrast to the high conductivity of the extra- and intracellular space. The application of a conveniently chosen current allows the measurement of an action voltage, whereby different phases can be distinguished (Fig. 7.1). The action voltage differs depending on the stimulus frequency, tissue type and location in the heart (Fig. 7.2).

An alternative procedure is the patch clamp technique, whereby the electrical behavior of a membrane patch restricted by the opening of a glass pipette

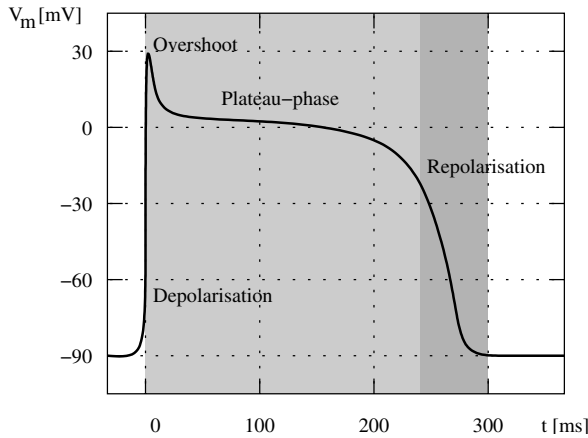


**Fig. 7.1.** Schematic illustration of action voltage  $V_m$  measured at membrane of cardiac myocyte (adapted from [152]). A stimulus current is applied in a myocyte with its membrane at resting voltage. After a fast depolarization the transmembrane voltage reaches positive values. Followed by a fast decrease the relatively long plateau phase is passed through. At their end the repolarization leads to a decrease commonly until the resting voltage is reached.

is registered. The patch is sealed to the glass pipette. Only two electrodes are used, one inside of the pipette and the other outside, near to the patch.

The most common used protocol for these measurements is the voltage clamp technique. Hereby, the voltage over the membrane is kept constant by supplying a convenient current. The voltage and the course of the current are registered. Commonly, in these measurements the voltage is varied stepwise, e.g. from  $-90\text{ mV}$  to  $20\text{ mV}$  in steps of  $10\text{ mV}$ .

The measurements are often performed in conjunction with the application of drugs and toxins, which allows the discrimination of the involved currents and channels. E.g. tetrodotoxin and tetraethylammonium block specifically sodium and potassium channels, respectively [154]. Furthermore, the variation of ionic concentrations and of the mechanical load offers additional insights [155].

A fundamental step in describing the electrophysiology of a cell membrane was performed by Hodgkin and Huxley, who measured and described quantitatively the active and passive electrical behavior of the axon membrane of giant squids [156]. Hereby, voltage clamp techniques as well as the variation of ionic concentrations and temperature were used to measure and discriminate currents through the membrane.

The measurements by Hodgkin and Huxley of the electrical behavior of the membrane as well as the numerous following experiments show significant nonlinearities of the membrane resistivity [156]. The nonlinearities can be attributed to the behavior of pores in the membrane, i.e. ionic channels

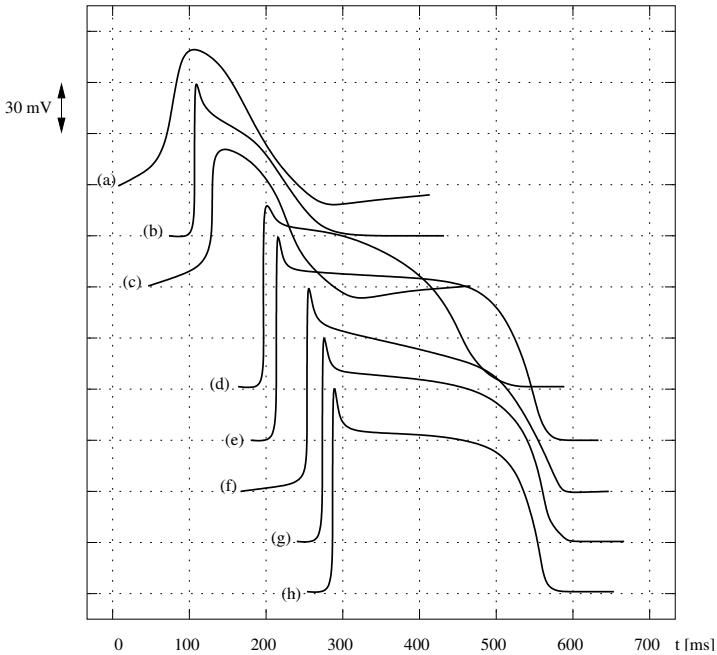


**Fig. 7.2.** Action voltages measured at membrane of human cardiac myocytes. The voltages at the membrane of myocytes from the (a) sinus node, (b) atrium, (c) atrioventricular node, (d) His bundle, (e) Tawara bundle branch, (f) Purkinje fibers, (g) subendocardial and (h) subepicardial ventricular myocardium are illustrated [153].

and pumps. Furthermore, concentration gradients over the membrane and ion specific permeabilities lead to measurable voltages, which can be dedicated to the behavior of semi-permeable membranes.

**Ionic Channels of the Cell Membrane.** Ionic channels exist in a wide variety in cell and intracellular membranes (Sect. 6.2.1). Their electrophysiological behavior can be measured with voltage clamp techniques of the whole cell, a membrane patch and a single channel. The observations show that a single channel flips randomly between a conducting and non-conducting state. Measurements of the stochastic opening and closing over a time period allow the assignment of channel specific probabilities of opening and closing. The transitions are performed in dependence of voltage, ionic concentrations, stretch and neurotransmitters. Often, a time influenced transition between the states can be found. A population of these channels acts in unison with the probabilities assigned to the single channel. The behavior of the population can be measured as the sum of the single channel behaviors.

*Sodium Channels.* Sodium channels are found to be responsible for the fast depolarization in myocytes of all vertebrates [87]. Measurements of sodium

channels with voltage clamp techniques show a fast transition to the high conductivity state if the voltage exceeds a threshold [156, 88]. Furthermore, the conductivity is found to be significantly time dependent. The conductivity decreases rapidly after activation. Sodium channels can be blocked specifically and reversibly by tetrodotoxin and saxitoxin [154].

*Potassium Channels.* Potassium channels show a large diversity in their molecular arrangement and in their electrophysiology. They are responsible for the repolarization of myocytes and neurons. Several types with a different time- and voltage-activated behavior are found in the heart [157]. Twenty different types are known only for voltage dependent channels, e.g. channels responsible for the ultra-rapid delayed rectifier current, the rapidly activating delayed rectifier current, the slowly activating delayed rectifier current, and the inward rectifier current. Furthermore, specific types of potassium channels are regulated by ATP [158] and cAMP [159]. Potassium channels can be blocked reversibly by tetraethylammonium, cesium, barium and dendrotoxins [154]. Heterogeneity of properties and densities of several potassium channels in the ventricular wall is reported for many species, e.g. cat, canine, and human [160, 161, 162, 163].

*Calcium Channels.* The sarcolemmal ionic channels with a high specificity for calcium show a voltage- and time-dependent behavior. They are discriminated by their electrophysiological behavior [89]. L-type calcium channels (dihydropyridines receptors) show relatively large and long lasting ion flow after activation. T-type channels show a tiny and transient ion flow. L-type channel blocking by magnesium, nickel, cadmium, and cobalt as well as regulation of the T-type channels by extracellular ATP was observed [154].

**Ionic Pumps of the Cell Membrane.** Pumps in the sarcolemma are e.g. the Na-K and calcium pump. The Na-K pump maintains the ionic gradients, which are largely influencing the transmembrane voltage. In a single procedure the Na-K pump transports three sodium ions out of and two potassium ions into the cell consuming ATP. The transport is found to be dependent on the intra- and extracellular sodium and potassium concentration as well as on transmembrane voltage and on temperature. The pump can be blocked specifically by quabain (strophantidin).

The sarcolemmal calcium pump transports calcium out of the cell dependent on the concentration of the intracellular calcium. The pump consumes ATP.

**Na-Ca Exchanger in the Cell Membrane.** Na-Ca exchangers are predominantly responsible for the transport of calcium out of the cell, which passed into the cell via the sarcolemmal calcium channels and leak currents [92]. In a single procedure three extracellular sodium ions are exchanged with a single intracellular calcium ion. A Na-Ca exchanger can also work in the

opposite direction, which is primarily found in the initial phase of excitation. Measurements show a dependence of the exchange capacity on the concentration of intra- and extracellular calcium and sodium as well as on the transmembrane voltage [164, 165]. The contribution of Na-Ca exchangers to the raise of intracellular calcium concentration during voltage clamp steps to 30 mV is reported to be ca. 10 % of the contribution of the L-type calcium channels [166]. A block is reported for small pH-values, flunarizine, and inorganic cations, e.g. cadmium, strontium and barium [68].

**Sarcoplasmic Reticulum.** The sarcoplasmic reticulum is an intracellular structure, which is enclosed by a membrane (Sect. 6.2.1). Studies, e.g. with antibodies, showed that the membrane contains calcium, potassium, chlorine and hydrogen ionic channel proteins as well as calcium pump proteins. The sarcoplasmic reticulum has a significant influence to the intracellular calcium handling. Calcium is pumped into the sarcoplasmic reticulum by the sarcoplasmic calcium pump and is released by the calcium release channels. Furthermore, leak calcium currents through the membrane are demonstrated. Insights in the electrophysiological behavior were primarily obtained by voltage clamp techniques of isolated vesicles.

*Calcium Release Channel.* The calcium release channel (ryanodine receptor) shows a high specificity for divalent cations [85]. The release channel is activated by approximately micro-molar cytoplasmic concentration of calcium and releases calcium buffered in the sarcoplasmic reticulum into the cytoplasm. This positive feedback mechanism is called calcium induced calcium release (CICR) [167]. An inhibition is reported by approximately milli-molar concentration of calcium. The channel is regulated by ryanodine and caffeine.

The activation of release channels is commonly result of calcium flux from the extracellular space into the cytoplasm through L-type calcium channels. The sarcoplasmic release and sarcolemmal L-type channels are located in close neighborhood. The summary calcium release occurs by concerted activation of many single channel release, leading to so-called calcium sparks [168, 86]. A refractory period of release channels is reported after their coherent and simultaneous activation. This refractoriness of circa 1 s is attributed to the entire sarcoplasmic reticulum and not found in small groups of functional units.

*Sarcoplasmic Calcium Pump.* The sarcoplasmic calcium pump, known also as sarcoplasmic  $Ca^{2+}$ -ATPase and SERCA (sarco-endoplasmatic reticulum calcium ATPase), transports calcium ions into the sarcoplasmic reticulum by usage of ATP. Two calcium ions are transported for each hydrolyzed ATP molecule. The sarcoplasmic calcium is buffered by the protein calsequestrin. The transport is regulated by the concentration of calcium, magnesium, ATP and the protein phospholamban as well as by pH-value [68, 169].

**Mitochondrion.** Mitochondria are intracellular organelles enclosed by a membrane (Sect. 6.2.1). The membrane contains calcium ionic channel and

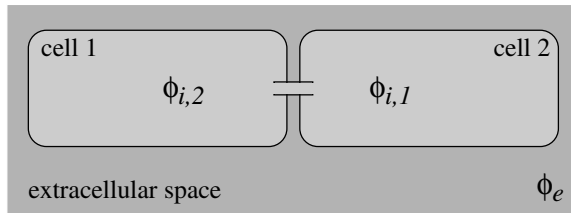


**Fig. 7.3.** Double cell voltage clamp technique. The conductivity of the gap junctions, which couple the intracellular space of adjacent myocytes, can be measured by clamping the potentials  $\phi_{i,1}$  and  $\phi_{i,2}$  of two adjacent cells. The voltages are clamped by two voltage sources with common reference potential  $\phi_e$ . The difference of the potentials delivers the voltage over the gap junction.

hydrogen pump proteins as well as sodium-calcium and hydrogen-sodium exchanger. Furthermore, hydrogen pumps are included. The sodium-calcium pump transports two sodium ion inside, while bringing one calcium ion to the cytosol. The hydrogen-sodium pump transports a hydrogen ion inside, while hauling one sodium ion outside.

**Gap Junctions.** Gap junctions are found to be the most important components of the electrical coupling between myocytes [94]. The gap junctions serve as a pathway, which transport electrical current from one cell to adjacent cells depending on the intracellular potentials. Hence, the gap junctions play a determinant role for the propagation of the electrical excitation through the myocardium.

The electrophysiological behavior of gap junctions can be determined by measurements with a variation of the before described voltage clamp methods, the so-called double cell voltage clamp technique (Fig. 7.3). The intracellular potential of each cell is clamped by a voltage source. The intercellular voltage is controlled by the two voltage sources with common reference potential. The voltages are registered in conjunction with the applied current, which offers the possibility to calculate the conductivity. The measurements show that the conductivity of gap junctions is dependent on their type and on the intercellular voltage. In the range between  $-50$  and  $50$  mV the variation is small for connexin43, which is the most abundant connexin in the mammalian myocardium.

Experiments were performed, which reveal that the gap junctions uncouple in the case of acute ischaemia and that the homogeneity and ordering of the gap junction distribution is decreased by chronic ischaemia. Also, chronic atrial arrhythmia and infective heart diseases changes the distribution pattern.

The conductivity of gap junctions can be decreased by halothane, heptanol and carbon dioxide [98]. A blocking is reported for low pH-values [95].



**Fig. 7.4.** Cell membrane and its approximation by resistor-capacitor circuit. The circuit consists of a nonlinear resistor  $R_m$  and a capacitor  $C_m$ . The voltage over the membrane  $V_m$  is hereby defined as the difference between the extracellular potential  $\phi_e$  and the intracellular potential  $\phi_i$

### 7.2.2 Modeling of Cellular Components

**Cell Membrane as Resistor-Capacitor Circuit.** The electrical behavior of a cell membrane can be approximated by a resistor-capacitor circuit with the nonlinear resistor  $R_m$  and the capacitor  $C_m$  (Fig. 7.4) [154]. The voltage over the membrane  $V_m$  is dependent on the charge  $Q$ :

$$V_m = \frac{Q}{C_m}$$

A change of the transmembrane voltage  $V_m$  can be described by the current flow  $I_C$ :

$$\frac{dV_m}{dt} = \frac{d}{dt} \frac{Q}{C_m} = \frac{I_C}{C_m}$$

assuming that the capacity  $C_m$  is constant over time. This equation is - adapted by definition of a summary current through the membrane - foundation of most electrophysiological models of membranes and cells.

The capacity of the sarcolemma is depending on its surface. A specific capacitance of approximately  $1 \mu F/cm^2$  is found in biological membranes.

The membrane resistor  $R_m$  is responsible for the discharge of the membrane by the current  $I_C$ . Using Ohm's law the resistor is determined by:

$$R_m = -\frac{V_m}{I_C}$$

**Equilibrium Voltages of Cell Membrane.** The description of the cell membrane as resistor-capacitor circuit neglects the phenomenon, that a voltage is generated across a semipermeable membrane between to regions with different ionic concentrations. Different equations, e.g. the Nernst and Goldman-Hodgkin-Katz equation, describe this voltage, which results from electrical and chemical forces. The equations are applied in the area of cellular electrophysiology. Hereby, the regions are the intra- and extracellular space with the semi-permeable cell enclosing membrane as border.



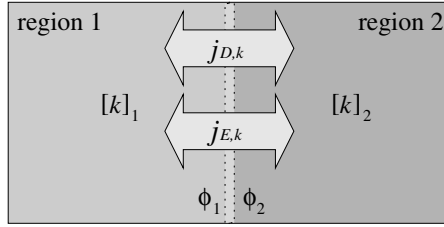


**Fig. 7.5.** Fluxes, potentials, and ionic concentrations of the Nernst equation. The equation describes the equilibrium voltage  $\phi_2 - \phi_1$  across the border of the two adjacent regions resulting from the ionic concentrations  $[k]_1$  and  $[k]_2$ . In equilibrium the flux of the ion  $k$  due to electrical forces  $\mathbf{j}_{E,k}$  and due to diffusion  $\mathbf{j}_{D,k}$  sums up to zero.

*Nernst Equation.* The Nernst equation describes the equilibrium voltage across the border of two regions resulting from gradients of ionic concentrations [154] (Fig. 7.5).

The Nernst equation determines the equilibrium voltage  $U$  by:

$$U = -\frac{RT}{z_k F} \ln \frac{[k]_1}{[k]_2}$$

with the gas constant  $R$ , Faraday's constant  $F$ , the concentrations in region 1  $[k]_1$  and in region 2  $[k]_2$  as well as the valence of the ion  $z_k$ . Furthermore, the equilibrium voltage  $U$  is linearly depending on the absolute temperature  $T$ .

The equilibrium is achieved when the total flux  $\mathbf{j}_k$  of the ion  $k$  through the border is zero. The Nernst equation takes into account two different fluxes: the ionic flux caused by diffusion  $\mathbf{j}_{D,k}$  and the ionic flux  $\mathbf{j}_{E,k}$  due to electrical forces (Fig. 7.5). Hence, the equilibrium is achieved if

$$\mathbf{j}_k = \mathbf{j}_{D,k} + \mathbf{j}_{E,k} = 0$$

is fulfilled. The ionic flux caused by diffusion  $\mathbf{j}_{D,k}$  is determined by the diffusion constant  $D_k$  and the gradient of the concentration  $[k]$ :

$$\mathbf{j}_{D,k} = -D_k \nabla [k]$$

Hereby, the diffusion coefficient is expressed as:

$$D_k = \frac{u_k RT}{|z_k| F}$$

The flux due to electrical forces  $\mathbf{j}_{E,k}$  is given by the ionic mobility  $u_k$ , the valence of the ion  $z_k$ , and the electrical potential  $\phi$ :

$$\mathbf{j}_{E,k} = -u_k \frac{z_k}{|z_k|} [k] \nabla \phi$$

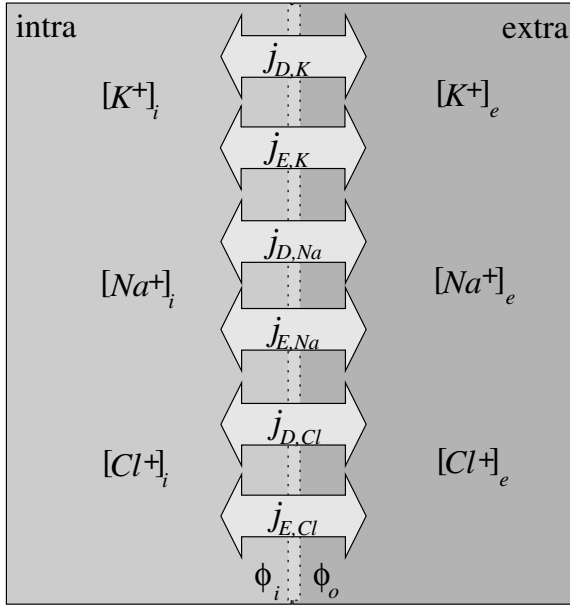


**Fig. 7.6.** Fluxes, potentials, and ionic concentrations of the Goldman-Hodgkin-Katz equation. The equation describes the equilibrium voltage  $\phi_i - \phi_o$  across a cellular membrane between the intra- and extracellular space resulting from the concentrations of potassium, sodium, and chlorine. In equilibrium the flux of the ions due to electrical forces  $j_E$  and due to diffusion  $j_D$  sums up to zero.

The flux due to electrical forces  $j_{E,k}$  can also be described by:

$$j_{E,k} = -D_k \frac{[k]z_k F}{RT} \nabla \phi$$

which leads to the Nernst-Planck equation delivering the total ionic flux  $j_k$ :

$$j_k = j_{D,k} + j_{E,k} = -D_k \left( \nabla [k] + \frac{[k]z_k F}{RT} \nabla \phi \right)$$

A restriction of the Nernst equation is caused by the inclusion of only one kind of ions. The approach is justifiable if the mobility of further kinds of ions is restricted or their concentrations are negligible.

*Goldman-Hodgkin-Katz Equation.* The Goldman-Hodgkin-Katz equation was developed to describe the equilibrium voltage  $U$  of a cellular membrane separating the intra- and extracellular space. The equation extends the Nernst equation by allowing the occurrence of multiple kinds of ions, which are determinants in cellular electrophysiology, i.e. potassium, sodium, and chlorine. A concentration for each kind of ions is assigned to the intra- and extracellular space as well as fluxes for each kind of ions caused by diffusion and electrical forces are allowed through the membrane (Fig. 7.6).

With the Goldman-Hodgkin-Katz equation the equilibrium voltage  $U$  is determined by:

$$U = -\frac{RT}{F} \ln \frac{P_K[K^+]_i + P_{Na}[Na^+]_i + P_{Cl}[Cl^-]_o}{P_K[K^+]_o + P_{Na}[Na^+]_o + P_{Cl}[Cl^-]_i}$$

from intra- and extracellular ionic concentrations, ionic permeabilities and the absolute temperature  $T$ . The permeability of the membrane for the potassium, Sodium, and Chloride ions is depicted by  $P_K$ ,  $P_{Na}$ , and  $P_{Cl}$ , respectively. The permeability of an ion  $k$  is expressed by:

$$P_k = \frac{D_k \beta_k}{h}$$

with the membrane thickness  $h$ , the diffusion coefficient  $D_k$  and the water-membrane partition coefficient  $\beta_k$ . The diffusion coefficient as well as the water-membrane partition coefficient are dependent on the type of membrane and kind of ion  $k$ .

A restriction of the Goldman-Hodgkin-Katz equation is that the membrane is presumed to be homogeneous, planar, and infinite as well as the distribution of the extra- and intracellular concentration is homogeneous. Further assumptions are that the electric field in the membrane is constant and the ions pass through the membrane independently [154].

**Ionic Channels.** The behavior of a single ionic channel can be modeled with states and functions describing the transition between the states. In the simplest case two states are assumed: an opened and a closed state. Assigned to these states is an opened probability  $O_i$  and a closed probability  $C_i$ , respectively, reflecting that the transition between the states is stochastic. The probabilities sum up to one. They are in the range between 0 and 1.

The change of the open probability  $O$  is determined by:

$$\frac{dO_i}{dt} = \alpha C_i - \beta O_i$$

with the rate constant  $\alpha$ , responsible for the transition from the closed to the opened state:  $C_i \Rightarrow O_i$ , and the rate constant  $\beta$ , concerned with the transition from the opened to the closed state:  $O_i \Rightarrow C_i$ . The rate constants depend on the type of ionic channel, transmembrane voltage, ionic concentration, stretch etc.. In equilibrium the change is zero:

$$\frac{dO_i}{dt} = 0$$

The macroscopic conductivity of a population of similar channels is specified by:

$$g_i = N_i O_i g_{i,max}$$

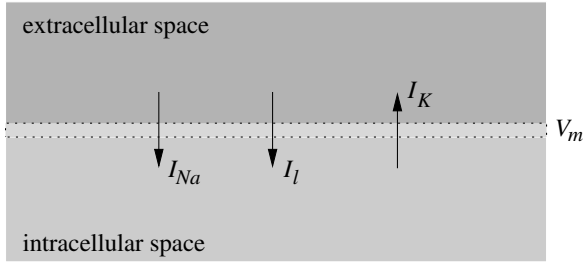


**Fig. 7.7.** Schematic diagram of the Hodgkin-Huxley model. The model calculates the currents  $I_{Na}$ ,  $I_K$ , and  $I_l$  as well as the transmembrane voltage  $V_m$ .

with the number of channels  $N_i$  and the maximal conductivity of the channel  $g_{i,max}$ .

The total current through a population of ionic channels is resulting from the difference between the transmembrane voltage  $V_m$  and the Nernst voltage  $E_i$ :

$$I_i = g_i(V_m - E_i)$$

with the conductivity  $g_i$ .

**Regional Concentrations and Current.** The time derivative of a regional concentration  $[k]$  for the ion  $k$  is calculated with:

$$\frac{\partial[k]}{\partial t} = -\frac{I_k}{z_k F V}$$

with the current  $I_k$  carrying ion  $k$ , the valence of the ion  $z_k$ , Faraday's constant  $F$  and the volume  $V$  of the region, where  $k$  is distributed.

**Model of Hodgkin and Huxley (1951).** The Hodgkin-Huxley model describes the dynamic electrophysiology of a giant squid axon membrane from measurements of the active and passive electrical behavior [156]. A foundation of the mathematical description is the Nernst Equation (7.2.2). Using the measurement data an equivalent circuit consisting of resistors, a capacity, and voltage sources was parameterized. Partly, the resistors were nonlinear time and voltage dependent.

The model allows to calculate ionic currents of different type passing through the axon membrane and the transmembrane voltage (Fig. 7.7 and Fig. 7.8). The transmembrane voltage  $V_m$  is defined as intracellular minus extracellular potential and the time derivative of  $V_m$  is described by:

$$\frac{\partial V_m}{\partial t} = -\frac{1}{C_m} (I_m + I_{stim})$$

with the membrane capacity  $C_m$ , the transmembrane current  $I_m$  and the stimulus current  $I_{stim}$ . The transmembrane current  $I_m$  reconstructed by the Hodgkin-Huxley model consists of

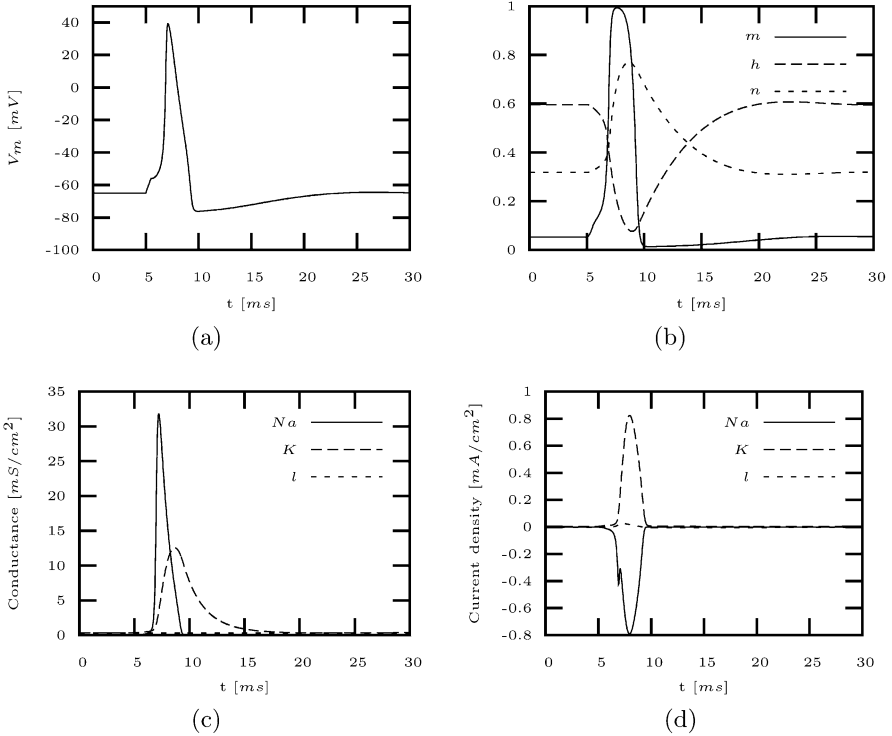


**Fig. 7.8.** Simulations with the Hodgkin-Huxley model. A stimulus current density of  $0.02 \text{ mA/cm}^2$  is injected at  $t = 5 \text{ ms}$  with a length of  $0.5 \text{ ms}$ . The stimulus leads to significant changes in (a) the transmembrane voltage, (b) the state variables for sodium and potassium channels, (c) the conductances, and (d) the transmembrane current densities of sodium, potassium and leakage.

$$I_m = I_{Na} + I_K + I_l$$

with the sodium current  $I_{Na}$ , the potassium current  $I_K$ , and the leakage current  $I_l$ . The leakage current  $I_l$  summarizes different ionic currents, primarily chloride ions. The currents are determined by the conductances  $g_{Na}$ ,  $g_K$ , and  $g_l$ , respectively, as well as by the difference between the transmembrane voltage and the equilibrium voltages  $E_{Na}$ ,  $E_K$ , and  $E_l$ , respectively:

$$I_{Na} = g_{Na}(V_m - E_{Na})$$

$$I_K = g_K(V_m - E_K)$$

$$I_l = g_l(V_m - E_l)$$

The conductance  $g_l$  is assumed to be constant, the other conductances vary with time and are voltage dependent. The ionic concentrations are supposed to be invariant leading to non-varying equilibrium voltages.

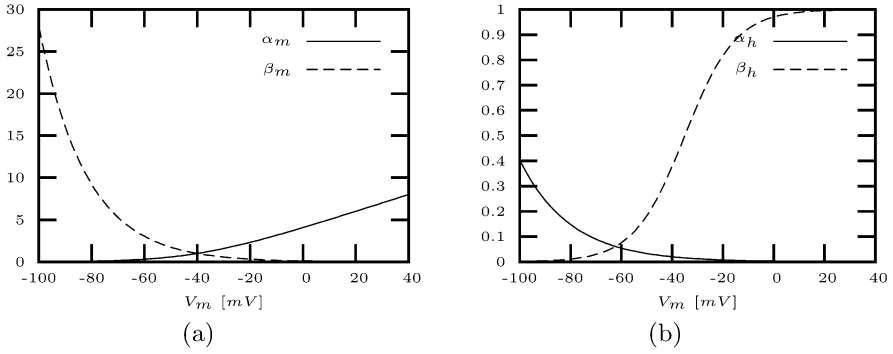


**Fig. 7.9.** Rate coefficients of sodium channels of the Hodgkin-Huxley model. The coefficients describe the voltage and time dependent changes of the state variables responsible for (a) the activation and (b) the inactivation of sodium channels.

The sodium conductivity  $g_{Na}$  is time and voltage dependent:

$$g_{Na} = m^3 h \bar{g}_{Na}$$

with the maximal conductance for sodium ions  $\bar{g}_{Na}$ , the dimensionless activation variable  $m$ , and inactivation variable  $h$ . The voltage dependent rate constants  $\alpha_m$ ,  $\beta_m$ ,  $\alpha_h$ , and  $\beta_h$  control the activation and inactivation variable:

$$\begin{aligned} \frac{dm}{dt} &= \alpha_m(1 - m) - \beta_m m \\ \frac{dh}{dt} &= \alpha_h(1 - h) - \beta_h h \end{aligned}$$

Fig. 7.9 shows the dependency on the rate constants  $\alpha_m$ ,  $\beta_m$ ,  $\alpha_h$ , and  $\beta_h$  to the transmembrane voltage  $V_m$ .

The biophysical motivated assumption of the weighting of the conductance  $g_{Na}$  by the state variables  $m$  and  $h$  was, that sodium ions can only flow through a sodium channel, if three similar, independent events lead to an opening and no blocking event occurred.

The potassium conductivity  $g_K$  is time and voltage dependent:

$$g_K = \bar{g}_K n^4$$

with the maximal conductance for potassium ions  $\bar{g}_K$  and the dimensionless state variable  $n$ , which is regulated by the voltage dependent rate constants  $\alpha_n$  and  $\beta_n$ :

$$\frac{dn}{dt} = \alpha_n(1 - n) - \beta_n n$$

Fig. 7.10 depicts the dependence of the rate constants  $\alpha_n$  and  $\beta_n$  to the transmembrane voltage  $V_m$ .

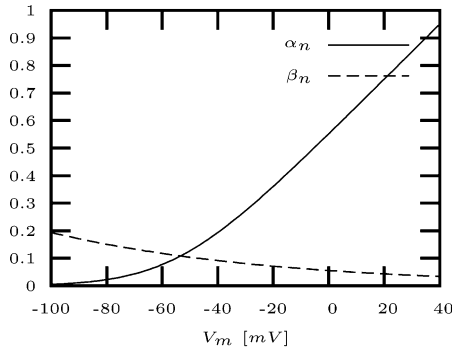


**Fig. 7.10.** Rate coefficients of potassium channels of the Hodgkin-Huxley model. The coefficients describe the voltage and time dependent changes of the state variables responsible for the activation of potassium channels.

The biophysical motivation of the weighting of the conductance  $g_K$  with the state variable  $n$  was the assumption, that potassium ions can only flow through a potassium channel, if four similar, independent events are involved in the opening process.

### 7.2.3 Models of Cardiac Myocytes

**Overview.** In the last years a large number of models of myocytes was constructed (table 7.1), with increasing abilities to describe the different electrophysiological mechanisms. Primarily, the models are produced from animal experiments using the mathematical formulations of Hodgkin and Huxley. The modeling approaches of the cell membrane, ionic channels and pumps, exchanger and intracellular components are combined to describe the behavior of a whole cell.

Modern models include detailed descriptions of the behavior of intracellular structures as well as of the influence of pharmaceuticals, neurotransmitters and mechanics. Some recently published models describe the human cellular electrophysiology.

In the following some electrophysiological models of cardiac cells are described. Their assumptions, principles and advances are presented. The overview is focused to models of ventricular myocytes. A model of Purkinje fibers and of cells from the sinoatrial node extend the overview. Special attention was attended to the handling of intracellular calcium, because of its importance for the coupling between electrical excitation and mechanical contraction.

**Model of Noble (1962).** The Noble model describes the electrophysiology of a Purkinje fiber by modifications of the Hodgkin-Huxley equations (Fig. 7.11) [170]. The selection of this cell type was caused by the relatively

**Table 7.1.** Electrophysiological models of cardiac cells.

Date	Publisher	Cell Type	Species	Reference
1962	Noble	Purkinje fiber	-	[170]
1975	McAllister, Noble, Tsien	Purkinje fiber	-	[171]
1977	Beeler, Reuter	ventricular myocardium	mammal	[172]
1980	Yanagihara, Noma, Irisawa	sinus node	rabbit	[173]
1982	Bristow, Clark	sinus node	rabbit	[174]
1983	Bristow, Clark	sinus node	rabbit	[175]
1984	Noble, Noble	sinus node	rabbit	[176]
1985	DiFrancesco, Noble	Purkinje fiber	mammal	[177]
1987	Hilgemann, Noble	atrial myocardium	rabbit	[178]
1990	Earm, Noble	atrial myocardium	rabbit	[179]
1991	Luo, Rudy	ventricular myocardium	mammal	[180]
1994	Luo, Rudy	ventricular myocardium	guinea pig	[181, 182]
1994	Demir, Clark, Murphey, Giles	sinus node	mammal	[183]
1996	Dokos, Celler, Lovell	sinus node	mammal	[184]
1996	Demir, O'Rourke, Tomaselli, Marban, Winslow	ventricular myocardium	canine	[185]
1996	Lindblad, Murphey, Clark, Giles	atrial myocardium	rabbit	[186]
1998	Courtemanche, Ramirez, Nattel	atrial myocardium	human	[187]
1998	Jafri, Rice, Winslow	ventricular myocardium	guinea pig	[188]
1998	Noble, Varghese, Kohl, Noble	ventricular myocardium	guinea pig	[189]
1998	Nygren, Fiset, Firek, Clark, Lindblad, Clark, Giles	atrial myocardium	human	[190]
1998	Priebe, Beuckelmann	ventricular myocardium	human	[191]
1999	Winslow, Rice, Jafri, Marbán, O'Rourke	ventricular myocardium	canine	[192, 193]
2000	Ramirez, Nattel, Courtemanche	atrial myocardium	canine	[194]
2000	Zhang, Holden, Kodama, Honjo, Lei, Varghese, Boyett	sinus node	rabbit	[195]
2002	Bernus, Wilders, Zemlin, Verschelde, Panfilov	ventricular myocardium	human	[196]
2003	Sachse, Seemann, Chaisaowong, Weiß	ventricular myocardium	human	[197]
2003	Seemann, Sachse, Weiß, Dössel	ventricular myocardium	human	[198]
2003	Ten Tusscher, Noble, Noble, Panfilov	ventricular myocardium	human	[199]



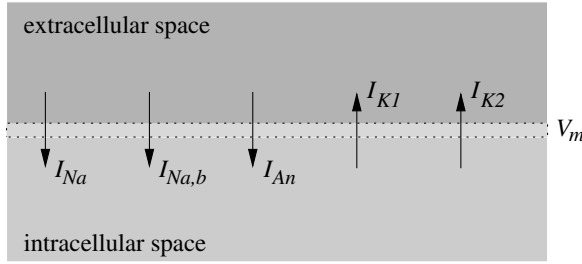


**Fig. 7.11.** Schematic diagram of the Noble model. The model calculates the currents  $I_{Na}$ ,  $I_{Na,b}$ ,  $I_{K1}$ ,  $I_{K2}$ , and  $I_{An}$  as well as the transmembrane voltage  $V_m$ .

large cellular size simplifying measurements and by the apparent resemblance of the electrophysiological behavior to nervous cells. A novel quality of the model was the decomposition of the sodium and potassium currents as well as the reconstruction of the pace-maker property in cells. As in the Hodgkin-Huxley model all ionic concentrations are supposed to be invariant. The conductances and the rate constants are adapted to fit to measurements and to take into account the decompositions.

The transmembrane current  $I_m$  reconstructed by the Noble model consists of

$$I_m = I_{Na} + I_{Na,b} + I_{K1} + I_{K2} + I_{An}$$

with the inward sodium current  $I_{Na}$ , the background sodium current  $I_{Na,b}$ , the outward potassium currents  $I_{K1}$  and  $I_{K2}$ , and the anion current  $I_{An}$  corresponding to the leak current of the Hodgkin-Huxley model.

The sodium current equations are similar to those from the Hodgkin-Huxley equations:

$$\begin{aligned} I_{Na} &= g_{Na}(V_m - E_{Na}) \\ g_{Na} &= m^3 h \bar{g}_{Na} \end{aligned}$$

with the time and voltage dependent conductance for sodium  $g_{Na}$ , the equilibrium sodium voltage  $E_{Na}$ , the dimensionless activation variable  $m$  and inactivation variable  $h$ . The sodium current is the principal determinant during the rising phase of the action voltage.

A background sodium current  $I_{Na,b}$  controlled by the constant background conductance  $g_{Na,b}$  is introduced:

$$I_{Na,b} = g_{Na,b}(V_m - E_{Na})$$

The outward potassium current is composed of two currents  $I_{K1}$  and  $I_{K2}$ . The current  $I_{K1}$  is time independent and decreases instantaneously when the membrane voltage increases:

$$I_{K1} = g_{K1}(V_m - E_K)$$

$$g_{K1} = 1.2e^{-\frac{V_m}{50}} + 0.015e^{\frac{V_m+90}{60}}$$

with the potassium conductance  $g_{K1}$  and the equilibrium potassium voltage  $E_K$ . The current  $I_{K2}$  is time and voltage dependent. Its description is similar to the Hodgkin-Huxley model:

$$I_{K2} = g_{K2}(V_m - E_K)$$

$$g_{K2} = \bar{g}_{K2}n^4$$

with the conductance for potassium  $g_{K2}$ , the maximal conductance for potassium  $\bar{g}_{K2}$ , and the dimensionless activation variable  $n$ . The voltage dependent rate constants  $\alpha_n$  and  $\beta_n$  specify the activation by

$$\frac{dn}{dt} = \alpha_n(1 - n) - \beta_n n$$

Their values are two order of magnitude smaller than in the Hodgkin-Huxley model, because of the slower onset of this current in Purkinje fibers.

The anion current equations are similar to those from Hodgkin-Huxley:

$$I_{An} = g_{An}(V_m - E_{An})$$

with the constant anion conductance  $g_{An}$  and the anion equilibrium voltage  $E_{An}$ .

**Model of Beeler and Reuter (1977).** The Beeler-Reuter model describes the electrophysiology of a mammalian ventricular myocyte based on measurements with the voltage-clamp method on multicellular preparations of cardiac muscle (Fig. 7.12) [172]. Variables of the model are the transmembrane voltage  $V_m$  and the intracellular calcium concentration  $[Ca^{2+}]_i$  as well as six activation and inactivation parameters  $m$ ,  $h$ ,  $j$ ,  $d$ ,  $f$ , and  $x_1$  controlling the conductance of the membrane. Each of these parameters is governed by a Hodgkin-Huxley equation with specifically chosen transfer rate coefficients.

The transmembrane current  $I_m$  reconstructed by the Beeler-Reuter model consists of

$$I_m = I_{Na} + I_{Na,b} + I_{K1} + I_{X1} + I_S$$

with:

Fast inward sodium current	$I_{Na}$
Background sodium current	$I_{Na,b}$
Outward potassium current	$I_{K1}$
Non-specific outward current, primarily potassium	$I_{X1}$
Non-specific inward current, primarily calcium	$I_S$

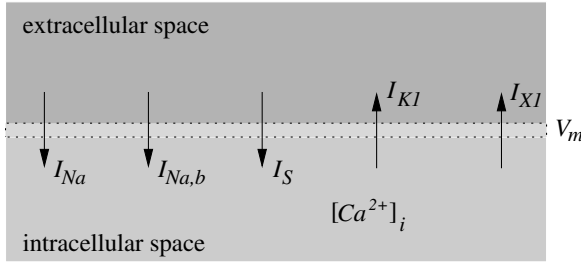


**Fig. 7.12.** Schematic diagram of the Beeler-Reuter model. The model calculates the transmembrane voltage  $V_m$ , the currents  $I_{Na}$ ,  $I_{Na,b}$ ,  $I_{K1}$ ,  $I_{X1}$ , and  $I_S$ , and the intracellular calcium concentration  $[Ca^{2+}]_i$ .

The time- and voltage-dependent inward sodium current  $I_{Na}$  is in particular responsible for the fast upstroke of the action voltage. The formulation is in parts adopted from the Hodgkin-Huxley and the Noble model:

$$I_{Na} = g_{Na} m^3 h j (V_m - E_{Na})$$

with the Nernst voltage of sodium  $E_{Na} = 50 \text{ mV}$ , the maximal sodium conductance  $g_{Na}$ , the activation parameter  $m$ , and the inactivation parameters  $h$  and  $j$ .

The sodium background current  $I_{Na,b}$  is time independent:

$$I_{Na,b} = g_{Na,b} (V_m - E_{Na})$$

with the background sodium conductance  $g_{Na,b}$  chosen to reproduce the measured steady sodium leakage current.

The time-independent and voltage-dependent outward potassium current  $I_{K1}$  is obtained by:

$$I_{K1} = 0.35 \left( \frac{4e^{0.04(V_m+85)} - 1}{e^{0.08(V_m+53)} + e^{0.04(V_m+53)}} + \frac{0.2(V_m + 23)}{1 - e^{-0.04(V_m+23)}} \right)$$

A large contribution of this current to the transmembrane current can be found at the plateau phase of the action voltage. The current is slowly deactivated and a determinant for the shape of the plateau phase of the action voltage.

The time-dependent and voltage-dependent outward current  $I_{X1}$  is mainly dedicated to the flow of potassium ions:

$$I_{X1} = 0.8 \, x1 \, \frac{e^{0.04(V_m+77)} - 1}{e^{0.04(V_m+35)}}$$

with the parameter  $x1$ . The current is slowly activated and responsible for the repolarization of the cell membrane.

The time- and voltage-dependent inward current  $I_S$  reflects the summary flow of different types of ions, but is primarily attributed to calcium ions:

$$I_S = g_s df(V_m - E_s)$$

with the Nernst voltage of calcium  $E_s = -82.3 - 13.0287 \ln [Ca^{2+}]_i$ , the maximal conductance  $g_s$ , the activation parameter  $d$ , and the inactivation parameter  $f$ . As the outward current  $I_{K1}$  the current  $I_S$  is slowly deactivated and a determinant for the shape of the plateau phase of the action voltage.

The concentration of the intracellular calcium  $[Ca^{2+}]_i$  is initially set to  $0.2 \mu M$ . The time derivative of  $[Ca^{2+}]_i$  is calculated with the inward current  $I_S$  by

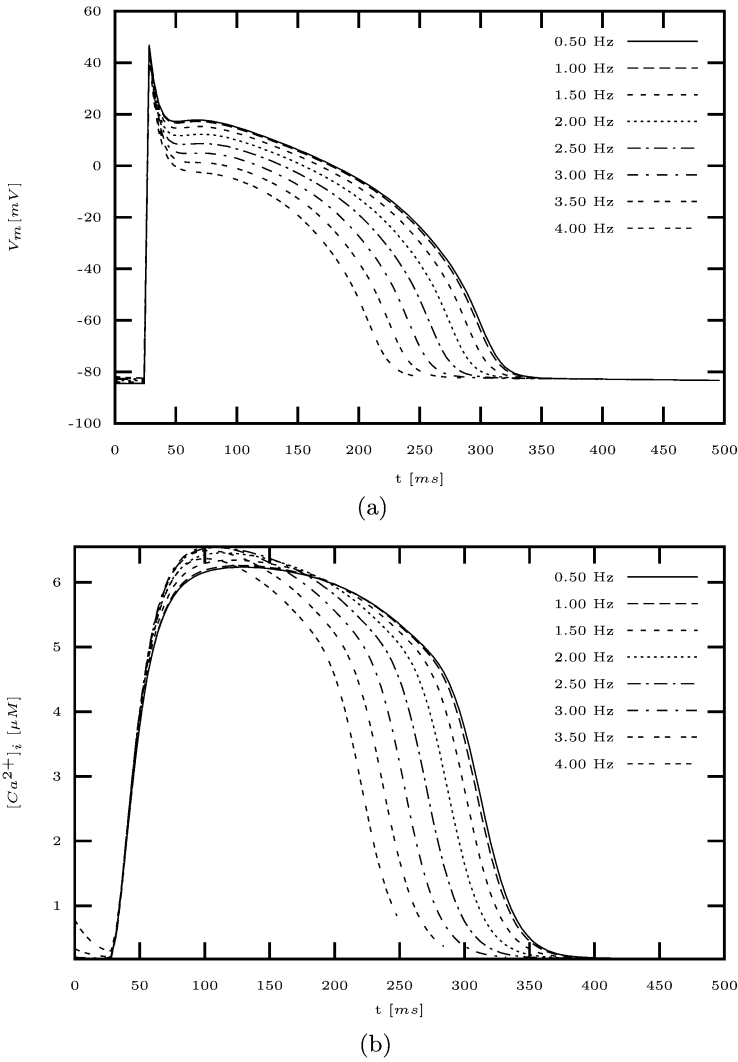
$$\frac{\partial [Ca^{2+}]_i}{\partial t} = -10^{-7} I_S + 0.07(10^{-7} - [Ca^{2+}]_i)$$

Fig. 7.13 (a) shows the transmembrane voltage calculated with the Beeler-Reuter model in dependency on different stimulus frequencies. An increase of the stimulus frequency in the range of  $[0.5 Hz \dots 3 Hz]$  leads to a decrease of the plateau voltage as well as of the action voltage duration. Simulations with lower frequencies lead to insignificant changes in the shape and duration of the action voltage. Simulations with higher frequencies using stimuli in the relative and absolute refractory period lead commonly to irregular shapes and durations.

Fig. 7.13 (b) depicts the intracellular calcium concentration  $[Ca^{2+}]_i$  resulting from simulations with different stimulus frequencies. An increase of the stimulus frequency in the range  $[0.5 Hz \dots 3 Hz]$  leads to a decreasing duration of the action voltage and of the calcium enhancement. Furthermore, the potential in and after the plateau phase is reduced.

The model of Beeler-Reuter reconstructs successfully the transmembrane voltage of ventricular myocytes. Major drawback is the neglect of important ionic channels, pumps and exchangers leading to deficiencies for the reconstruction of many phenomena. Furthermore, the model overestimates the intracellular calcium concentration  $[Ca^{2+}]_i$  significantly, which can be attributed e.g. to the neglect of buffering mechanisms by troponin and calmodulin.

**Model of Luo and Rudy Phase-1 (1991).** The Luo-Rudy phase-1 model describes the electrophysiology of a ventricular cell from guinea pig based primarily on data from single-cell and single-channel measurements (Fig. 7.14) [180]. The model is a succession of the Beeler-Reuter model using similar formulations e.g. for the fast sodium current and the slow inward current. Variables of the model are the transmembrane voltage  $V_m$  and the intracellular calcium concentration  $[Ca^{2+}]_i$  as well as seven activation and inactivation parameters  $m$ ,  $h$ ,  $j$ ,  $d$ ,  $f$ ,  $x$ , and  $k1$ . Each of these parameters is governed by a Hodgkin-Huxley equation with specifically chosen transfer rate coefficients.



**Fig. 7.13.** Simulations with the Beeler-Reuter model. (a) Transmembrane voltage  $V_m$  and (b) intracellular calcium concentration  $[Ca^{2+}]_i$  are dependent on the stimulus frequency. For each frequency a single course is visualized. The cell is activated by applying a current at  $t = 25$  ms with a length of 3 ms.

The transmembrane current  $I_m$  of the Luo-Rudy phase-1 model consists of

$$I_m = I_{Na} + I_{si} + I_K + I_{K1} + I_{Kp} + I_b$$

with:

Fast inward sodium current	$I_{Na}$
Slow inward current	$I_{si}$
Time-dependent potassium current	$I_K$
Time-independent potassium current	$I_{K1}$
Plateau potassium current	$I_{Kp}$
Background potassium current	$I_b$

The transfer rate coefficients for the activation of the fast inward sodium current  $I_{Na}$  were adjusted to achieve an upstroke velocity  $\frac{\partial V_m}{\partial t}$  of  $400 \frac{mV}{s}$ . A novelty of the model was the introduction of the plateau potassium current  $I_{Kp}$  activated at high potentials.

The model allows the reproduction of supernormal activity, defined as larger than normal excitability during or after the repolarization phase, and of Wenckebach periodicity, defined as periodic, stimulus frequency dependent activation failure.

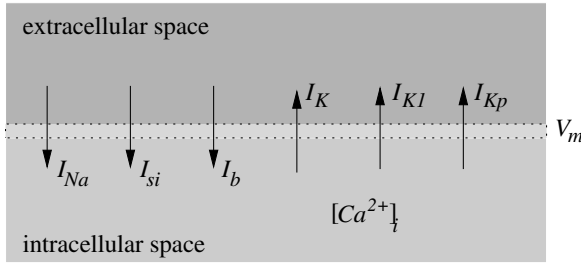


**Fig. 7.14.** Schematic diagram of the Luo-Rudy phase-1 model. The model calculates the transmembrane voltage  $V_m$ , the currents  $I_{Na}$ ,  $I_{si}$ ,  $I_K$ ,  $I_{K1}$ ,  $I_{Ko}$ , and  $I_b$ , and the intracellular calcium concentration  $[Ca^{2+}]_i$ .

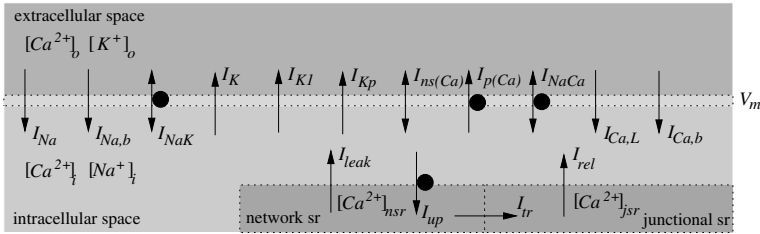
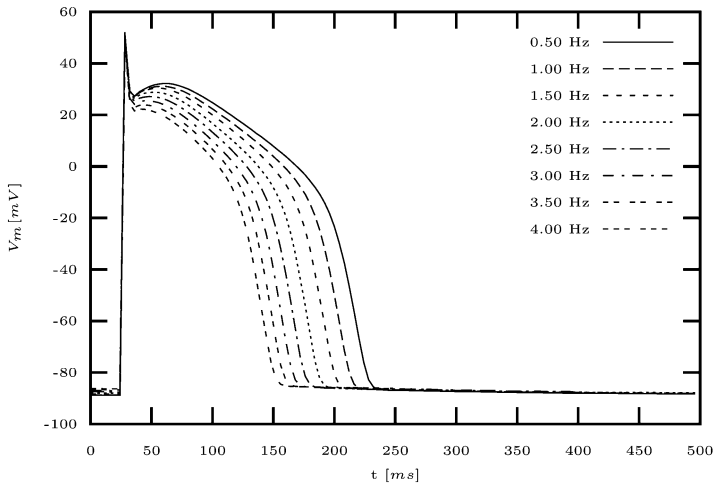
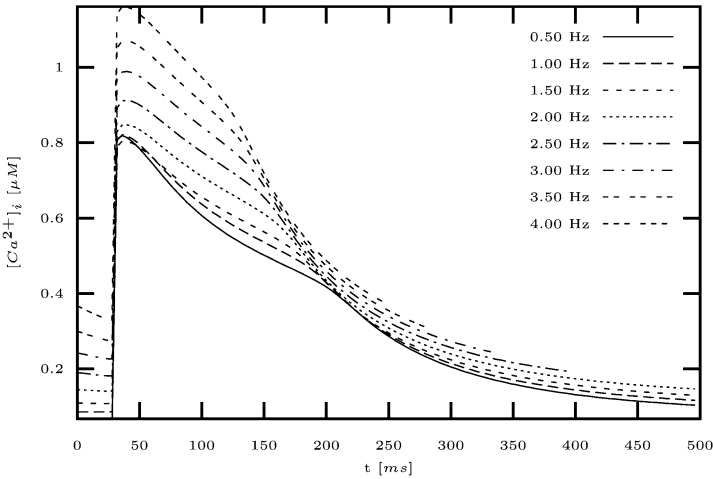


**Fig. 7.15.** Schematic diagram of the original Luo-Rudy phase-2 model. The model calculates the transmembrane voltage  $V_m$ , eleven currents through the sarcolemma and four currents of the sarcoplasmic reticulum (sr). Furthermore, two extracellular and four intracellular concentrations are updated.



(a)



(b)

**Fig. 7.16.** Simulations with an enhanced Luo-Rudy phase-2 model. (a) Transmembrane voltage  $V_m$  and (b) intracellular calcium concentration  $[Ca^{2+}]_i$  are dependent on the stimulus frequency. For each frequency a single course of the transmembrane voltage and intracellular calcium concentration, respectively, is visualized.

**Model of Luo and Rudy Phase-2 (1994).** The Luo-Rudy phase-2 model is an extension of the phase-1 model and describes the electrophysiology of a ventricular cell (Fig. 7.15) [181, 182]. The model is constructed primarily from single-cell and single-channel measurements of guinea pig ventricular cells. The extension consists mainly of a reformulation of the calcium handling, i.e. the intracellular currents describing quantitatively the calcium mechanics of the

sarcoplasmic reticulum. Different enhancements and adaptations of the model exist.

The transmembrane current  $I_m$  of the original phase-2 model consists of

$$I_m = I_{Na} + I_{Ca,L} + I_K + I_{K1} + I_{Kp} + I_{NaCa} + I_{NaK} \\ + I_{ns(Ca)} + I_{p(Ca)} + I_{Ca,b} + I_{Na,b}$$

with:

Fast inward sodium current	$I_{Na}$
Currents through L-type calcium channel ( $Ca^{2+}$ , $Na^+$ , $K^+$ )	$I_{Ca,L}$
Time-dependent potassium current	$I_K$
Time-independent potassium current	$I_{K1}$
Plateau potassium current	$I_{Kp}$
Na-Ca exchanger current	$I_{NaCa}$
Na-K pump current	$I_{NaK}$
Non-specific calcium-activated current	$I_{ns(Ca)}$
Sarcolemmal calcium pump	$I_{p(Ca)}$
Background calcium current	$I_{Ca,b}$
Background sodium current	$I_{Na,b}$

The model includes a representation of the sarcoplasmic reticulum by two subcompartments, the network and the junctional sarcoplasmic reticulum. The subcompartments serve for the buffering of calcium ions. The intracellular calcium mechanisms are governed by four currents:

inward calcium current to network sarcoplasmic reticulum	$I_{up}$
outward calcium current from network sarcoplasmic reticulum	$I_{leak}$
calcium current between network and junctional sarcoplasmic reticulum	$I_{tr}$
outward calcium current from junctional sarcoplasmic reticulum	$I_{rel}$

The current  $I_{up}$  represents a pump mechanism transporting calcium ions from the cytoplasm to the network sarcoplasmic reticulum. The calcium ions are transferred via a leak current  $I_{leak}$  back to the cytoplasm and via the current  $I_{tr}$  to the junctional sarcoplasmic reticulum. Thenceforth, the calcium is released to the cytoplasm with a calcium activated current  $I_{rel}$ .

The model allows the reconstruction of early (EAD) and delayed after-depolarization (DAD) as well as triggered and rhythmic activity, which are arrhythmogenic single cell phenomena [200]. The EAD is defined as a depolarizing after-voltage beginning before the completion, the DAD as a depolarizing after-voltage beginning after the completion of the repolarization.

**Model of Demir, Clark, Murphey and Giles (1994).** The Demir-Clark-Murphey-Giles model describes the electrophysiology of a rabbit sinoatrial node cell (Fig. 7.17) [183]. The model is based on whole cell recordings from enzymatically isolated single cells of the border zone of the sinus node. The



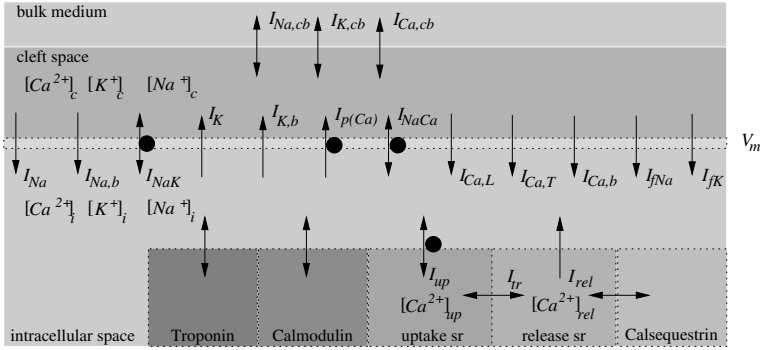


**Fig. 7.17.** Schematic diagram of the Demir-Clark-Murphey-Giles model. The model calculates the transmembrane voltage  $V_m$ , twelve currents through the sarcolemma, three current from the cleft space to the bulk medium, and three currents of the sarcoplasmic reticulum (sr). Furthermore, three cleft and five intracellular concentrations are updated.

internal concept is derived from the work of DiFrancesco and Noble [177] as well as Hilgeman and Noble [178].

The transmembrane currents  $I_m$  of the Demir-Clark-Murphey-Giles model are described by:

$$I_m = I_{Na} + I_{Ca,T} + I_{Ca,L} + I_K + I_{fK} \\ + I_{fNa} + I_{Na,b} + I_{K,b} + I_{Ca,b} + I_{NaK} + I_{NaCa} + I_{p(Ca)}$$

with:

Inward sodium current	$I_{Na}$
Transient calcium current	$I_{Ca,T}$
Long-lasting calcium current	$I_{Ca,L}$
Time- and voltage dependent delayed rectifier potassium current	$I_K$
Hyper-polarization-activated potassium current	$I_{fK}$
Hyper-polarization-activated sodium current	$I_{fNa}$
Background sodium current	$I_{Na,b}$
Background potassium current	$I_{K,b}$
Background calcium current	$I_{Ca,b}$
Na-K pump current	$I_{NaK}$
Na-Ca exchanger current	$I_{NaCa}$
Calcium pump current	$I_{p(Ca)}$

The activation rate coefficients of the inward sodium currents are adapted to consider the low upstroke velocity  $\frac{\partial V_m}{\partial t}$  of sinoatrial node cells. The model includes two hyper-polarization-activated currents  $I_{fK}$  and  $I_{fNa}$ . Hyper-polarization-activated currents are of importance for any model of pacemaker

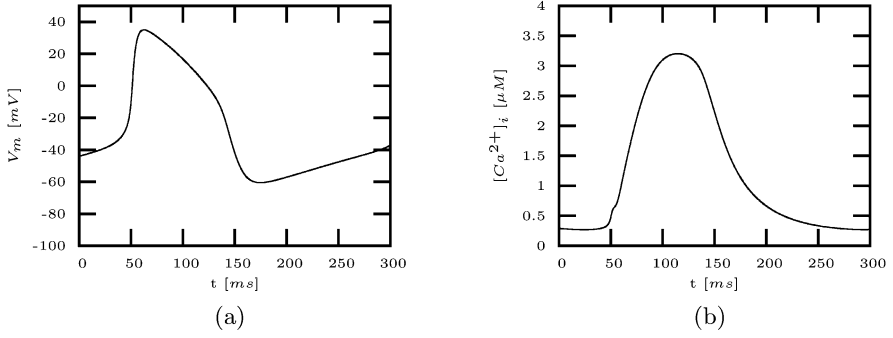


**Fig. 7.18.** (a) Transmembrane voltage  $V_m$  and (b) intracellular calcium concentration  $[Ca^{2+}]_i$  calculated with Demir-Clark-Murphey-Giles model.

activity. The currents increase the transmembrane voltage after a repolarization. An automatic depolarization process is initiated after exceeding of the threshold voltage (Fig. 7.18).

**Model of Priebe and Beuckelmann (1998).** The Priebe-Beuckelmann model describes the electrophysiology of a human ventricular myocyte [191]. The model was used as a tool to explore therapeutic interventions on the electrical excitability of myocardium. The model is a descendant of the Luo-Rudy phase-2 model, which was parameterized with data from measurements of transmembrane voltage, ionic currents and concentrations in human myocytes [201].

The transmembrane currents  $I_m$  of the Priebe-Beuckelmann model are described by:

$$I_m = I_{Na} + I_{Ca,L} + I_{to} + I_{Kr} + I_{Ks} \\ + I_{K1} + I_{NaCa} + I_{NaK} + I_{Na,b} + I_{Ca,b}$$

with:

Inward sodium current	$I_{Na}$
Long-lasting calcium current	$I_{Ca,L}$
Transient outward potassium current	$I_{to}$
Time- and voltage dependent delayed rectifier potassium current	$I_{Kr}$
Time- and voltage dependent delayed rectifier potassium current	$I_{Ks}$
Inward rectifier potassium current	$I_{K1}$
Na-Ca exchanger current	$I_{NaCa}$
Na-K pump current	$I_{NaK}$
Background potassium current	$I_{Na,b}$
Background calcium current	$I_{Ca,b}$

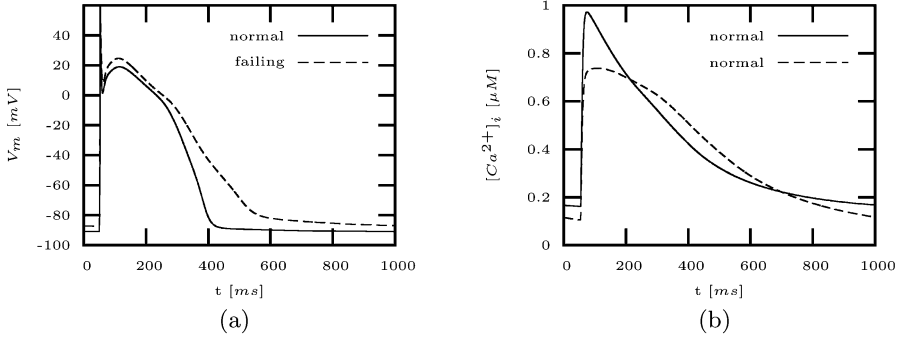


**Fig. 7.19.** Simulations with the Priebe-Beuckelmann model of human ventricular myocytes. The reconstructed course of (a) transmembrane voltage  $V_m$  and (b) intracellular calcium concentration  $[Ca^{2+}]_i$  show differences in normal and failing myocytes. Failing myocytes feature prolonged duration of action voltage and intracellular calcium transients.

Models exist for normal and failing myocytes (Fig. 7.19). The model of failing myocytes differs in several parameters from the model of normal myocytes: reduced conductivity for transient output potassium current  $g_{to,max}$ , reduced conductivity for inward rectifier current  $g_{K1,max}$ , increased conductivity for calcium background current  $\bar{G}_{Ca,b}$ , reduced conductivity of sodium background current  $\bar{G}_{Na,b}$ , down-regulation of Na-K pump  $\bar{I}_{NaK}$ , up-regulation of Na-Ca exchanger  $k_{NaCa}$ , down-regulation of network sarcoplasmic reticulum calcium pump  $\bar{I}_{up}$ , and decreased calcium leak of network sarcoplasmic reticulum  $K_{leak}$ .

A variant of the model exists using only six state variables, which allows an efficient calculation of excitation propagation [196]. The model shows significant numerical advantages, but neglects intracellular calcium handling and several further components.

The Priebe-Beuckelmann model was adapted in subsequent work to take recent measurement data from humans into account and to integrate it with tension development models [197, 198]. Adaptations were made for both normal and failing myocytes concerning the intracellular calcium handling, i.e. NSR  $Ca^{2+}$  uptake,  $Ca^{2+}$  background current, and Na-Ca exchanger. Further adaptations were made to reconstruct the heterogeneity of several components over the ventricular wall, i.e. transient outward potassium current  $I_{to}$ , the delayed rectifier potassium currents  $I_{Kr}$  and  $I_{Ks}$ , and inward rectifier potassium current  $I_{K1}$ .

**Model of Noble, Varghese, Kohl and Noble (1998).** The Noble-Varghese-Kohl-Noble model describes the electrophysiology of a ventricular cell of guinea pig (Fig. 7.20). The model includes effects on ionic channels by the concentration of ATP and acetylcholine (ACh) as well as by stretching. Furthermore, a force generation model is included. A description of the diadic

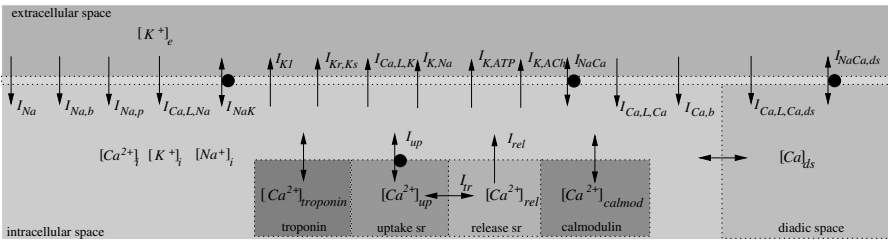


**Fig. 7.20.** Schematic overview of the Noble-Varghese-Kohl-Noble model. The model calculates the transmembrane voltage  $V_m$ , the currents through the sarcolemma to the intracellular space and the currents of the sarcoplasmic reticulum (sr). Furthermore, intra- and extracellular concentrations are updated.

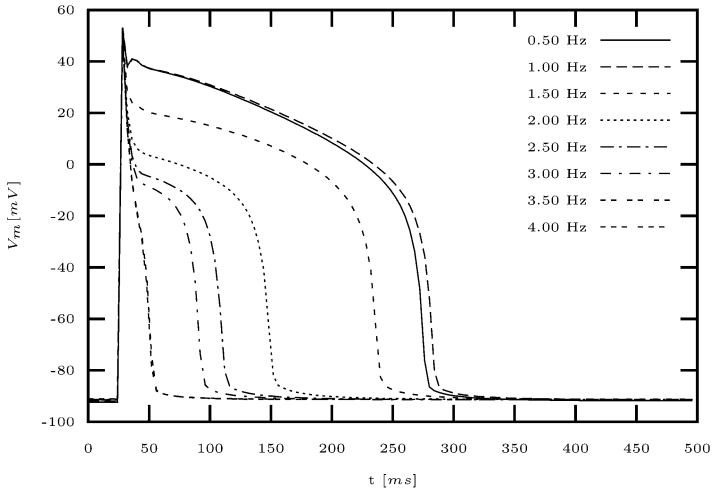
space is incorporated. Different variants and configurations of the model exist. The following description is based on [189, 202, 203] and focused on the electrophysiological part of the model.

Hereby, the transmembrane currents are described by:

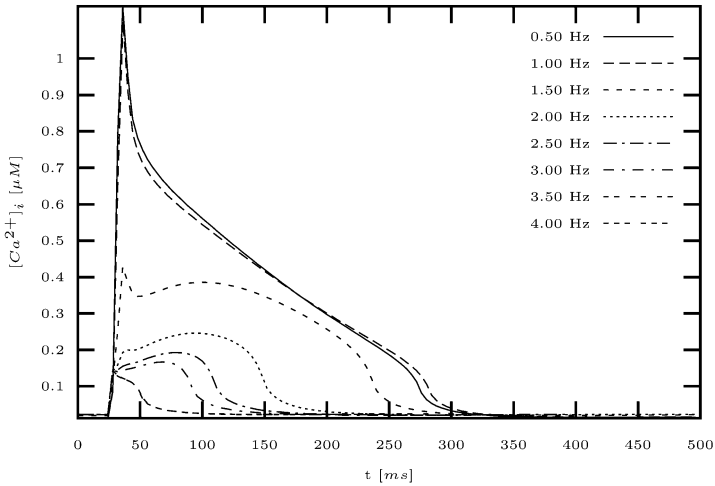
$$\begin{aligned}
I_m = & I_{Na} + I_{Na,b} + I_{Na,p} \\
& + I_{K1} + I_{Kr} + I_{Ks} + I_{K,ATP} + I_{K,ACh} \\
& + I_{Ca,b} + I_{Ca,L,K} + I_{Ca,L,Na} + I_{Ca,L,Ca} \\
& + I_{Ca,L,K,ds} + I_{Ca,L,Na,ds} + I_{Ca,L,Ca,ds} \\
& + I_{NaK} + I_{NaCa} + I_{NaCa,ds} \\
& + I_{stretch}
\end{aligned}$$

with:

Fast sodium current	$I_{Na}$
Background sodium current	$I_{Na,b}$
Voltage dependent sodium current	$I_{Na,p}$
Time-independent potassium current (background)	$I_{K1}$
Time-dependent, delayed potassium currents	$I_{Kr}, I_{Ks}$
Sodium dependent potassium current	$I_{K,Na}$
ATP-dependent potassium current	$I_{K,ATP}$
ACh-dependent potassium current	$I_{K,ACh}$
Background calcium current	$I_{Ca,b}$
Currents through L-type calcium channels	$I_{Ca,L,Ca}, I_{Ca,L,Na},$ $I_{Ca,L,K}$
L-type calcium current into the diadic space	$I_{Ca,L,Ca,ds}$
Na-K pump current	$I_{NaK}$
Na-Ca exchanger current	$I_{NaCa}$
Na-Ca exchanger current for diadic space	$I_{NaCa,ds}$
Stretch activated currents	$I_{stretch}$



(a)



(b)

**Fig. 7.21.** Simulations with the Noble-Varghese-Kohl-Noble model. (a) Transmembrane voltage  $V_m$  and (b) intracellular calcium concentration  $[Ca^{2+}]_i$  are dependent on the stimulus frequency. For each frequency a single course of the transmembrane voltage and the calcium concentration is visualized.

Fig. 7.21 shows the influence of stimulus frequency to the course of the transmembrane voltage  $V_m$  and intracellular calcium concentration  $[Ca^{2+}]_i$ . Hereby, stretch activated currents are neglected. With higher stimulus frequency the resting voltage is increased and the duration of the action voltage is decreased.

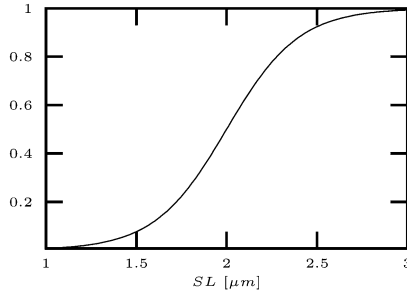


**Fig. 7.22.** Stretch function for weighting of ion conductances in dependence of sarcomere length  $SL$ . The sarcomere length  $SLHST$  of half maximal activation is set to  $2 \mu m$ , the steepness parameter  $SACSL$  to 2.

*Intracellular Mechano-Electric Feedback.* The Noble-Varghese-Kohl-Noble model includes dependencies of electrophysiological parameters on the length or tension of the sarcomere. The mechano-electric feedback is realized by introducing

- selective and non selective stretch-activated ion conductances
- a modulation of calcium binding to troponin
- a modulation of sarcoplasmic leak current

The following description of the mechanisms is restricted to the length dependencies of the electrophysiological parameters. The length or stretch dependent formulation is of advantage for the coupling with deformation models.

*Stretch-activated ion conductances.* Two models are proposed to calculate stretch-activated ion conductances and to reconstruct stretch activated currents. In both models the ion conductances are weighted by the sarcomere length  $SL$  with the stretch function

$$fstretch(SL) = \frac{1}{1 + e^{-2SACSL(SL-SLHST)}}$$

with the steepness parameter  $SACSL$  and the sarcomere length  $SLHST$  at which half maximal activation occurs (Fig. 7.22).

The first model describes the summary stretch current  $I_{stretch}$  with a non-specific  $I_{Ns-stretch}$  and an anion stretch current  $I_{An-stretch}$ :

$$I_{stretch} = I_{Ns-stretch} + I_{An-stretch}$$

The currents  $I_{Ns-stretch}$  and  $I_{An-stretch}$  are determined by the stretch function  $fstretch$  dependent on the sarcomere length  $SL$ , the maximal conductivities  $g_{Ns-stretch}$  and  $g_{An-stretch}$ , respectively, and the equilibrium voltages  $E_{Ns-stretch}$  and  $E_{An-stretch}$ , respectively:

$$I_{Ns-stretch} = fstretch(SL) g_{Ns-stretch} (V_m - E_{Ns-stretch})$$

$$I_{An-stretch} = fstretch(SL) g_{An-stretch} (V_m - E_{An-stretch})$$

The second model subdivides the summary stretch current  $I_{stretch}$  in a sodium  $I_{Na-stretch}$ , a potassium  $I_{K-stretch}$ , a calcium  $I_{Ca-stretch}$ , and an anion stretch current  $I_{An-stretch}$ :

$$I_{stretch} = I_{Na-stretch} + I_{K-stretch} + I_{Ca-stretch} + I_{An-stretch} \quad (7.1)$$

Hereby, the stretch currents are calculated as described in the simple model with the stretch function  $f_{stretch}$ , the maximal conductivities and the equilibrium voltages:

$$\begin{aligned} I_{Na-stretch} &= f_{stretch}(SL) g_{Na-stretch} (V_m - E_{Na}) \\ I_{K-stretch} &= f_{stretch}(SL) g_{K-stretch} (V_m - E_K) \\ I_{Ca-stretch} &= f_{stretch}(SL) g_{Ca-stretch} (V_m - E_{Ca}) \\ I_{An-stretch} &= f_{stretch}(SL) g_{An-stretch} (V_m - E_{An-stretch}) \end{aligned}$$

The second model describes the stretch current obviously more detailed regarding the different types of ions and herewith offers the advantage to update quantitatively the sodium, potassium and calcium concentrations.

*Modulation of calcium binding to troponin C.* The binding of intracellular calcium to troponin C is modulated by stretch:

$$\begin{aligned} \frac{\partial [Ca^{2+}]_{troponin}}{\partial t} &= \alpha_{troponin} e^{\gamma_{trop,SL} SL} ([troponin] - [Ca^{2+}]_{troponin}) [Ca^{2+}]_i \\ &\quad - \beta_{troponin} [Ca^{2+}]_{troponin} \end{aligned}$$

with the concentration of calcium bound to troponin C  $[Ca^{2+}]_{troponin}$ , the total troponin concentration  $[troponin]$ , the intracellular calcium concentration  $[Ca^{2+}]_i$ , the transfer rates  $\alpha_{troponin}$  and  $\beta_{troponin}$ , and the parameter  $\gamma_{trop,SL}$ . The stretch is defined by the sarcomere length  $SL$ .

*Modulation of sarcoplasmic reticulum leak current.* The calcium leak current  $I_{rel}$  from the sarcoplasmic reticulum to the cytoplasm is divided in a stretch dependent and an independent part:

$$I_{rel} = \left( \frac{f_{activator}}{f_{activator} + 0.25} \right)^2 k_{mca2} [Ca^{2+}]_{rel} + J_{SR-leak} e^{\gamma_{SR,SL} SL}$$

The current is controlled independently of stretch by the state variable  $f_{activator}$ , the parameter  $k_{mca2}$  and the sarcoplasmic calcium concentration  $[Ca^{2+}]_{rel}$ . The stretch dependent part is calculated with the sarcomere length  $SL$ , the experimentally determined parameters  $\gamma_{SR,SL}$  and  $J_{SR-leak}$ .

*Simulations.* Two sets of simulations were performed to examine the influence of static and dynamic stretch [204]. The influence of static stretch of different strength was tested by initiation of excitation via injection of a convenient current with a duration of 3 ms. The phenomena of dynamic stretch were

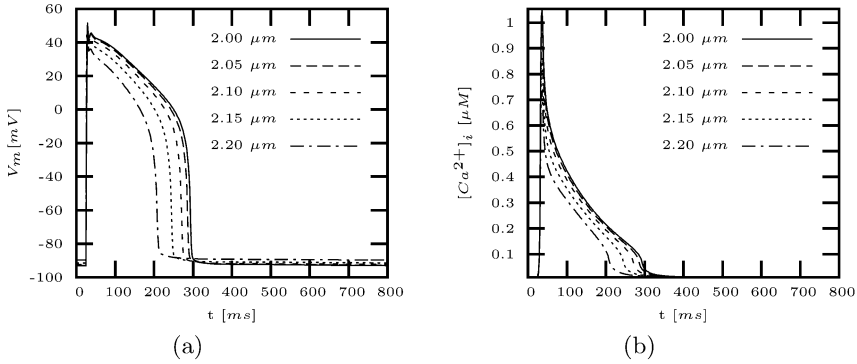


**Fig. 7.23.** Simulations with varied static length of sarcomere. (a) Transmembrane voltage and (b) calcium concentration in the cytoplasm dependent on length of sarcomere calculated with Noble-Varghese-Kohl-Noble model. The cell is excited by applying a stimulus current at  $t = 25$  ms with a length of 3 ms. The sarcomere length ranges from 2.0 to 2.2  $\mu m$ . The default length of the sarcomere is 2  $\mu m$ . The stimulus frequency was set to 1 Hz.

examined with different stretch impulses and durations. The application of stretch starts in the diastolic phase. In both sets of simulations the calculated model variables were stored and processed.

The complex stretch model (equation 7.1) is parameterized and used in the following simulations. The parameterization was performed by fitting data measured in single guinea pig ventricular myocytes [155] with methods similar to those presented in [205]. The parameters are  $SACSL = 7$ ,  $SLHST = 2.4$   $\mu m$ ,  $g_{Na-stretch} = 15$  nS,  $g_{K-stretch} = 30$  nS,  $g_{Ca-stretch} = 0.1$  nS,  $g_{An-stretch} = 15$  nS, and  $E_{An-stretch} = -20$  mV. The simulations deliver information concerning the mechanisms of mechano-electric feedback.

The influence of static stretch on the course of the transmembrane voltage and the intracellular calcium concentration is illustrated in Fig. 7.23 and Fig. 7.24. Hereby, the stretch amplitude is specified by the length of the sarcomere with a default of 2  $\mu m$ . The resting voltage as well as the progression of the action voltage are dependent on the length of the sarcomere ranging from 1.6 to 2.2  $\mu m$ . The resting voltage as well as the course of the action voltage are dependent on the length of the sarcomere ranging from 2.0 to 2.2  $\mu m$ . The resting voltage increases and the duration of the action voltage decreases with larger sarcomere length. Both effects can be attributed to the raise of the sarcolemmal conductances. The maxima of the transmembrane voltage are independent of stretch.

The influence of mechanical stretch impulses is depicted in Fig. 7.25 and Fig. 7.26. In the presented simulations the stretch amplitude and duration were varied. Once again, the stretch amplitude was specified by the length of the sarcomere with a default of 2  $\mu m$ . Depending on the amplitudes and



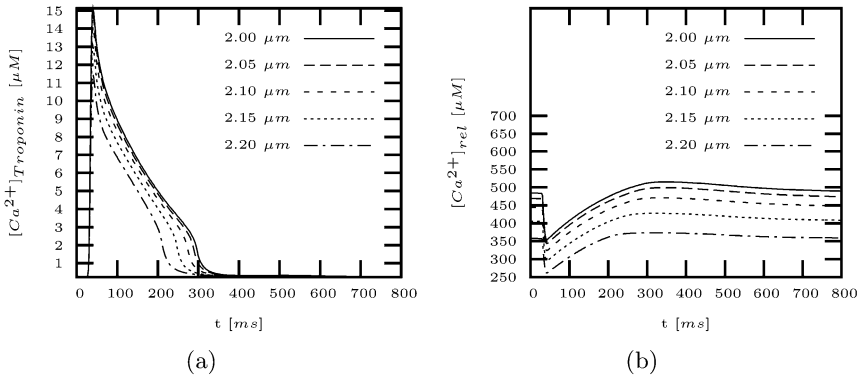


**Fig. 7.24.** Simulations with varied static length of sarcomere (continued). (a) concentration of calcium bound to troponin C and (b) concentration of calcium in the release part of the sarcoplasmic reticulum dependent on length of sarcomere calculated with Noble-Varghese-Kohl-Noble model. The cell is excited by applying a stimulus current at  $t = 25$  ms with a length of 3 ms. The sarcomere length ranges from 2.0 to 2.2  $\mu m$ . The default length of the sarcomere is 2  $\mu m$ . The stimulus frequency was set to 1 Hz.

the length an effect ranging from a small change of the resting voltage to an excitation of the cell was achieved.

The simulation presented in Fig. 7.25 (a) shows the initiation of an action impulse by a relatively small stretch duration only for large sarcomere length. The simulations with sarcomere length 2.5  $\mu m$  show an increase in the duration of the action impulse with the exception of the results with a relatively long stretch duration depicted in Fig. 7.26 (a) and (b).

The initiation of early afterdepolarizations (EAD) is apparent in Fig. 7.25 (d) and 7.26 (a) for sarcomere lengths 2.4 and 2.5  $\mu m$ , and for length 2.4  $\mu m$ , respectively. The classification of the EADs was performed using the description of [206] by examination of the activation and inactivation gates of the L-type calcium channels during the plateau phase.

All these effects are primarily attributed to the raise of the sarcolemmal conductances by stretch. The stretch dependence of intracellular structure influences the course of the transmembrane voltage only to a small degree.

## 7.3 Excitation Propagation

### 7.3.1 Experimental Studies

**Measurement Systems.** The propagation of electrical excitation in the heart is commonly measured by temporal and spatial registration of voltages resulting from cardiac current flow. Cellular processes generate the current

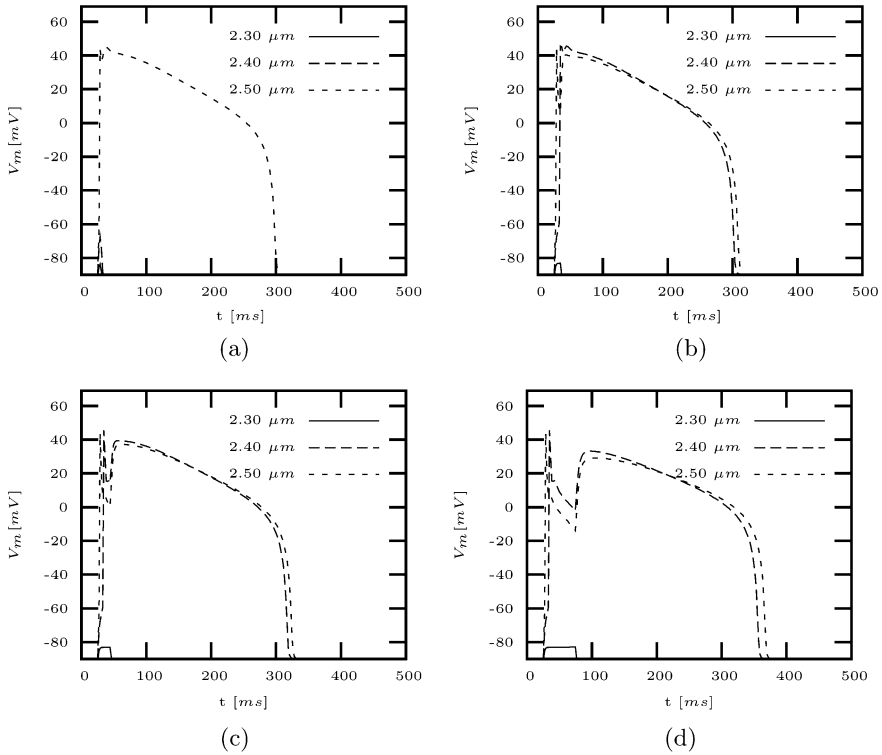


**Fig. 7.25.** Simulation of initiation of action impulse by dynamic stretch simulated with Noble-Varghese-Kohl-Noble model. At  $t = 25$  ms a mechanical stretch of (a) 5 ms, (b) 10 ms, (c) 20 ms, and (d) 50 ms was performed delivering a sarcomere length from 2.3 to 2.5  $\mu\text{m}$ . The default length of the sarcomere is 2  $\mu\text{m}$ . Some combinations of stretch and length lead to action impulses, others increase the transmembrane voltage insufficiently for activation.

flow, i.e. the transmembrane current responsible for the de- and repolarization of myocytes (Sect. 7.2.1). Electrocardiographic, magnetocardiographic and optical systems were developed to register the propagation of electrical excitation.

Electrocardiographic systems measure so-called electrocardiograms, which are registered via electrodes and amplified for further processing [207]. An electrocardiogram consists of voltages, which are assigned to different points in time. These voltages can be alluded to the intra- and extracellular domain as well as over the membrane.

Magnetocardiographic systems produce magnetocardiograms, whereby the magnetic field resulting from the electrical current flow is registered [208]. This current flow is composed of intracellular, extracellular and transmembrane currents.

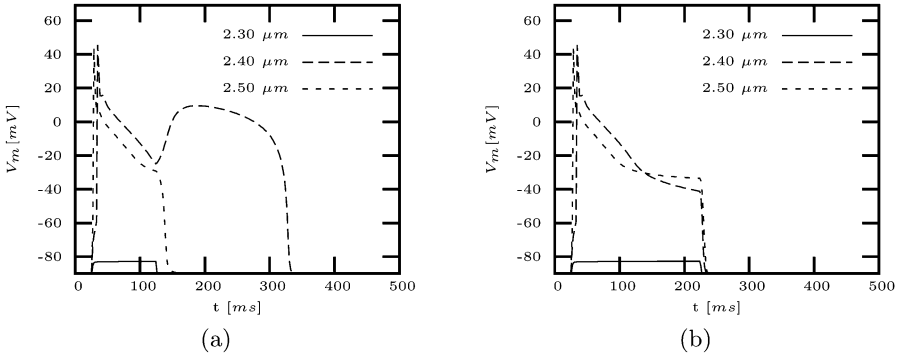


**Fig. 7.26.** Simulation of initiation of action impulse by dynamic stretch simulated with Noble-Varghese-Kohl-Noble model (continued). At  $t = 25 \text{ ms}$  a mechanical stretch of (a)  $100 \text{ ms}$ , and (b)  $200 \text{ ms}$  was performed delivering a sarcomere length from  $2.3$  to  $2.5 \text{ }\mu\text{m}$ . The default length of the sarcomere is  $2 \text{ }\mu\text{m}$ .

Optical systems work in conjunction with voltage sensitive dyes, video recordings and image processing. Commonly, the course of transmembrane voltage is scanned at surfaces of extracorporated hearts and multicellular preparations.

The electrocardiography is the primary tool in clinical diagnosis. Hereby, the electrocardiograms are registered via electrodes, amplified and commonly visualized for visual analysis. A distinction commonly made for medical measurement systems concerns the placement of the registration. Hereby, extra- and intracorporal systems are distinguished.

Of diagnostic importance is the extracorporal registration via electrodes at the body surface, whereby different arrangements of electrodes are used to produce e.g. the leads of Einthoven, Goldberger and Wilson. The extracorporal registration delivers voltages resulting from the distribution of current sources in the heart and the conductivity distribution in the body (Fig. 7.27). A spatial discrimination of the excitation process is possible by analysis with numerical methods and by usage of background knowledge concerning the electrophysiology of the heart. Nevertheless, an automated, computer-based analysis is still topic of research.

Alternatively, in clinical diagnosis intracorporal methods allow a simplified spatial discrimination and deliver additional information. Hereby, voltages are measured e.g. at the subepicardial myocardium via multi-electrode socks [209] and in the endocardial cavity via multi-electrode catheters [210, 211].

Furthermore, the propagation can be observed directly at cellular and multicellular level, e.g. by registration of the

- transmembrane voltages with voltage clamp techniques (Sect. 7.2.1)
- intercellular current flow through gap junctions with double cell voltage clamp techniques (Sect. 7.2.1)
- extracellular voltages in the near-by of an excited structure (Fig. 7.28).

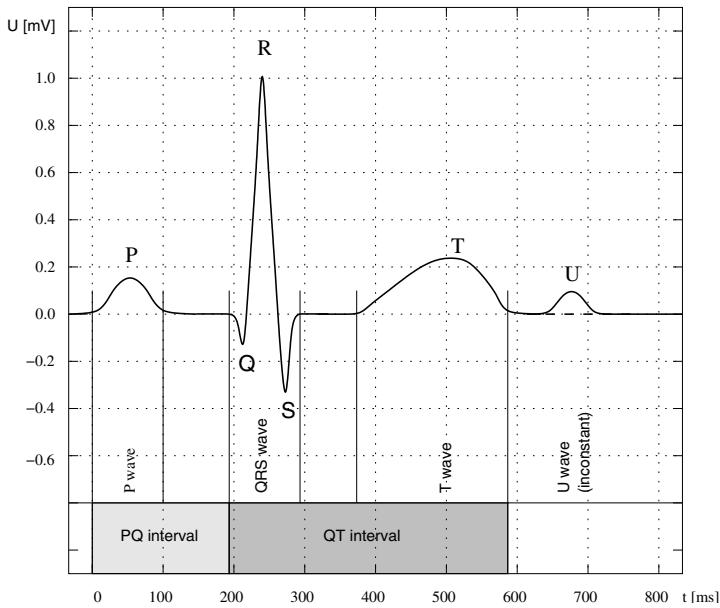


**Fig. 7.27.** Exemplary electrocardiogram for physiological excitation propagation in normal, adult humans. Commonly, the P wave takes less than 100 ms, the PQ interval less than 200 ms, and the QRS wave less than 100 ms. The duration of the QT interval is dependent on the cycle rate. E.g. for a cycle rate of  $70 \text{ min}^{-1}$  a duration of 320 – 390 ms is observed [152].

The registration, analysis and automatic classification of electrocardiograms is a basic function of many biomedical instruments and software packages. E.g. the stimulus delivery of pacemakers as well as external and implanted defibrillators are controlled by features extracted from electrocardiograms. Also, the measurement of excitation propagation velocity necessitates the detection of activation times in electrograms.

**Mechanisms.** The mechanisms of macroscopic excitation propagation through the heart was examined by various studies since the begin of the twentieth century [128, 124, 117, 126]. The studies showed, that the normal electrical excitation is cyclical and precedes the mechanical contraction. The chronological order of activation was found to be similar in hearts of mammals.

As initiator of the physiological excitation serves the sinus node. Then, the excitation propagates over the right atrium to the atrioventricular node and via the Bachmann bundle to the left atrium. The atrioventricular node delays the propagation. Afterwards, the His bundle, the fast conducting Tawara bundle branches and the subendocardially located Purkinje fibers are activated. Subsequently, the excitation passes to the subendocardial ventricular myocardium, wherefrom the excitation traverses the ventricles to their epicardial surface.

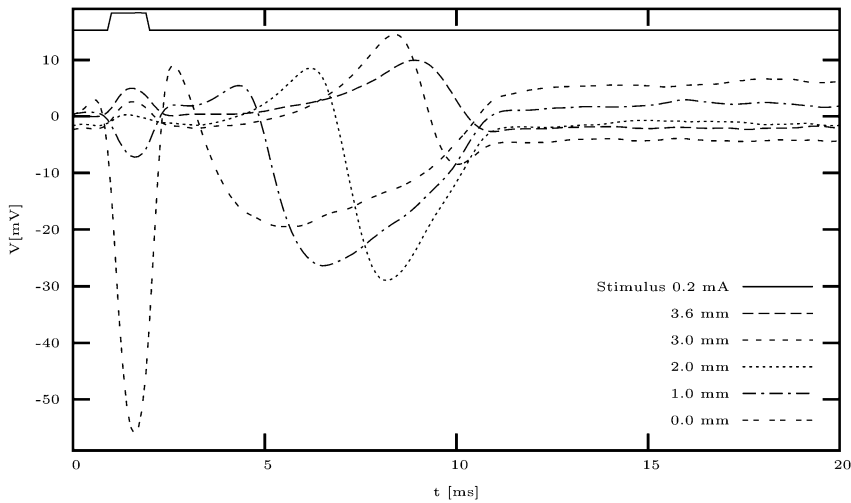


**Fig. 7.28.** Electrograms measured at surface of papillary muscle. The papillary muscle was excised from a rabbit's right ventricle and placed in a flow-through bath. The muscle is fixed at both ends, i.e. the onset of the tendon and proximal to its former attachment to the ventricle wall. A stimulus was given at  $t=1$  ms with a length of 1 ms proximal to the former attachment. Electrograms were measured at several positions along the muscle, i.e. near to the stimulus electrode, indicated by 0 mm, and in a distance of 1, 2, 3, and 3.6 mm. Activation times can be detected by analysing the electrograms, e.g. by searching for maximal negative slopes in the region after the stimulus artefact.

The excitation propagation process can be registered with extracorporeal electrodes (Fig. 7.27). The propagation through the atria corresponds to the P wave. The propagation through the ventricles is reflected by the QRS wave, their repolarization by the T wave.

Further studies of different types, e.g. with double cell voltage clamp techniques (Sect. 7.2.1) and genetically modified cells [97], showed that the intercellular excitation propagation is resulting from a flow of current primarily through gap junctions. The current flow is depending on the differences of the intracellular potential. Hence, the cellular electrophysiology, i.e. the upstroke velocity of the transmembrane voltage, determines the excitation velocity. Primarily, sodium and potassium ions serve as charge carrier.

Coupling via gap junctions between cardiac myocytes and fibroblasts is reported, e.g. by connexin45 in the sinoatrial node and connexin43 in rat ventricular cell cultures [212, 213]. The electrophysiological implications of this coupling are still topic of research.

Experimental studies of the mechanisms of microscopic propagation of electrical excitation through the myocardium showed different phenomena depending on the scale of observation [214, 215]. In the scale of single cells a discontinuous, stochastic propagation is found resulting from the irregular

cellular shape and the inhomogeneous gap junction distribution. In a larger scale a continuous, anisotropic propagation is observed. The anisotropy is resulting from the myocyte orientation dependent, averaged distribution of gap junctions.

A variety of phenomena can be initiated by experiments, whereby specifically timed and located electrical stimulus sequences are applied [216, 217, 218]. Similar stimulus sequences applied via endocardial catheter electrodes are used in clinical electrophysiological examinations for an evaluation of the heart.

An important arrhythmogenic phenomenon is the unidirectional block for excitation propagation, which can be found in excitable media commonly resulting from static or dynamic inhomogeneities. A unidirectional block can be generated with a suitably located and timed stimulus of the excitable media, e.g. of the atrial and ventricular myocardium. The stimulus is suitably located and timed, if the stimulus is located with one part in a non-excitable area, with the other in an excitable area. The non-excitability of the area results from an electrophysiological cellular status in which the cell cannot be activated by an early secondary stimulus. In this case the excitation propagates in the direction opposite to the blocked area.

Depending on the dimension of the excitable media, different phenomena resulting from a unidirectional block can be observed: In a one-dimensional domain the block leads to a propagation in the opposite direction, while normally a stimulus is followed by two propagation fronts in each direction. A block in a non-homogeneous two-dimensional area can lead to a rotating wave around obstacles, which is reported e.g. in the right and left atrium [217, 218]. The block can also lead to single or multiple spiral waves. The spiral waves can rotate freely, no obstacles or channels of muscle structures are necessary. The three-dimensional equivalent for spiral waves are scroll waves.

### 7.3.2 Modeling Approaches

Different modeling approaches of the excitation propagation in the myocardium can be distinguished depending on the representation of the microscopic and macroscopic anatomy as well as depending on the approximation of the cellular electrophysiology.

Modeling approaches that use only macroscopic information allow the combining of cells and their common treatment. In contrast, models using microscopic anatomical information at a cellular level split cells in components, which are separately treated.

In the last years different approaches for the macroscopic excitation propagation were developed:

- cellular automata
- reaction diffusion systems

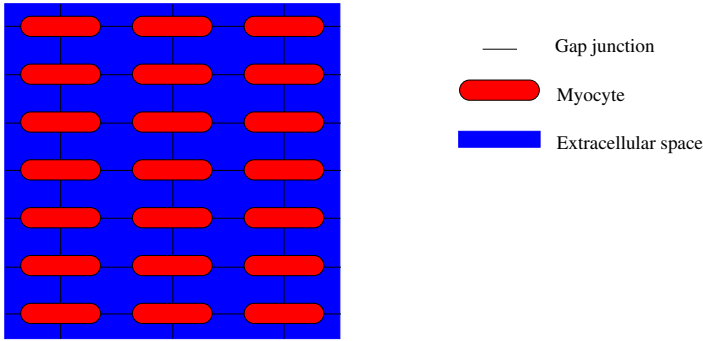


**Fig. 7.29.** Modeling of electrical intercellular coupling. Adjacent myocytes are coupled via gap junctions and through the extracellular space.

Microscopic and macroscopic models allow the inclusion of anisotropic effects resulting from the orientation of myocytes, e.g. by using conductivity tensors. Commonly, the methods are applied on a one-, two- or three-dimensional lattice (Fig. 7.29), whereby each cell's intracellular space is coupled directly only with the intracellular space of adjacent cells.

**Microscopic Models.** Microscopic models use anatomical information of the cellular architecture acquired with microscopy to reconstruct the excitation propagation in a region of the myocardium [219, 214]. The region is divided in different areas, which are assigned to the intra- and extracellular space, the membrane of myocytes and capillaries. The membrane areas include an electrophysiological description, i.e. the sarcolemmal ionic currents from a cell model. The current flow between the areas is modeled with Ohm's law using resistors.

The approach allows the inclusion of irregularities of the cellular architecture as well as inhomogeneities of the orientation and distribution of gap junctions. Hence, anisotropic effects are implicitly included.

Microscopic models allow the reconstruction of experimental results, whereby the inhomogeneous microstructure of the myocardium is of importance. An example therefore is the discontinuous excitation propagation found at cellular level [214, 215]. The microscopic modeling of the myocardium is restricted to a small volume, because of the high expense to describe each single cell with a number of complex and coupled elements.

### 7.3.3 Cellular Automata

Cellular automata are applied as models of natural processes in various disciplines, e.g. in physics, chemistry, biology, and medicine. A large number of different cellular automata were developed to model the excitation process in the heart [220, 221, 222, 223, 224, 225, 226, 227, 228, 142, 37]. Cellular models

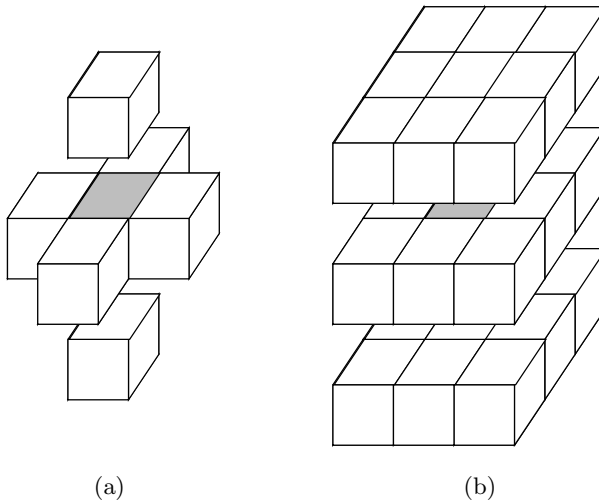


**Fig. 7.30.** Three-dimensional neighborhood of cells in cellular automaton. The grey labeled central cell communicates with (a) 6 and (b) 26 neighbors (from [37]).

were used in the early work of Wiener and Rosenblueth (1946) to describe phenomena of excitation propagation in two-dimensional sheets of cardiac muscle [220] and of Moe et al. (1964) to model atrial fibrillation [221]. Recently published works showed that cellular automata are capable of efficient simulation of excitation propagation in the whole heart. Furthermore, tissue specific and stimulus frequency dependent courses of the transmembrane voltage as well as tissue specific anisotropy of excitation velocities are taken into account in these simulations [225, 228, 142].

A cellular automaton can be divided in two components [229, 230]:

- regular, discrete, infinite network representing the underlying spatial structure.
- finite automaton working at each node (so-called cell) of the network.

Each cell communicates with a finite set  $N$  of other cells. The number and the arrangement of the cells with which a cell communicates determines the neighborhood of the cellular automaton. Classical neighborhoods are the nearest neighbors neighborhoods of von Neumann or Moore. In case of three-dimensional cellular automata these are the 6- and 26-neighborhood, respectively (Fig. 7.30). The neighborhood determines the shape of the wave front (Fig. 7.31). The set  $N$  is usually fixed and is an ordered subset of the set of all cells  $Z$ .

The communication between cells is performed in a local, deterministic, uniform and synchronous way. Hence, the global evolution of the system is predetermined running the cellular automaton along discrete time steps [229].



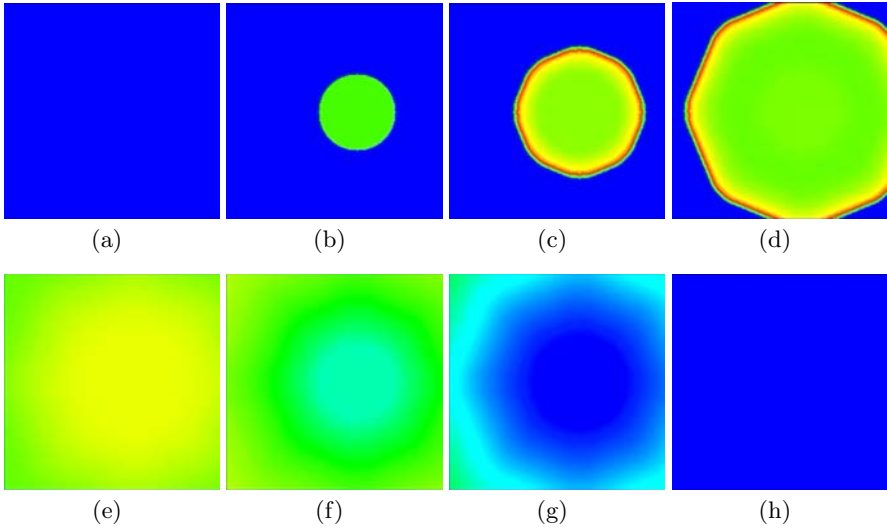


**Fig. 7.31.** Excitation wave simulated with a cellular automaton in a three-dimensional slice of  $256 \times 256 \times 3$  elements with a size of  $0.2 \text{ mm} \times 0.2 \text{ mm} \times 0.2 \text{ mm}$  modeling the electrophysiology of atrial cells. The simulated transmembrane voltage is color coded illustrated at different time steps. (a) Initially, the area is in the resting state with all cells at resting voltage. (b) A stimulus was applied followed by (c-g) a wave propagating over the area. The shape of the wave front is resulting from the 26-neighborhood used in the cellular automaton for the communication between cells. (h) Finally, the area is returned to the resting state with all cells at resting voltage.

*Model of Werner, Sachse, Seemann, and Dössel.* The three-dimensional automaton simulates the propagation of electrical excitation with models ranging from areas of myocardium up to the whole heart [227, 231, 142, 37]. Anisotropy of the myocardium and frequency dependent changes of the course of the transmembrane voltages are taken into account.

As underlying spatial structure anatomical models of the myocardium and of the whole heart can be used. E.g. the whole heart model used in the subsequently described simulations consists of a classified anatomical tissue data set (section 6.4.5) derived from the Visible Man data set, a myocyte orientation data set and a specialized cardiac conduction system tree. While the myocyte orientation data set has only an impact on the local transition function, the conduction system tree varies the neighborhood of the cells located at the nodes of the tree. Hence, unlike classical cellular automata, the neighborhood  $N$  varies. For cells located at the nodes of the tree the 26 fixed neighbors are extended by the set of successors and one predecessor defined by the conduction system tree. However, most of the cells have a fixed set  $N_{fixed}$  of 26 neighbors, whereas only for a very small number of the cells, approximately 0.01 %, the neighborhood  $N$  varies.

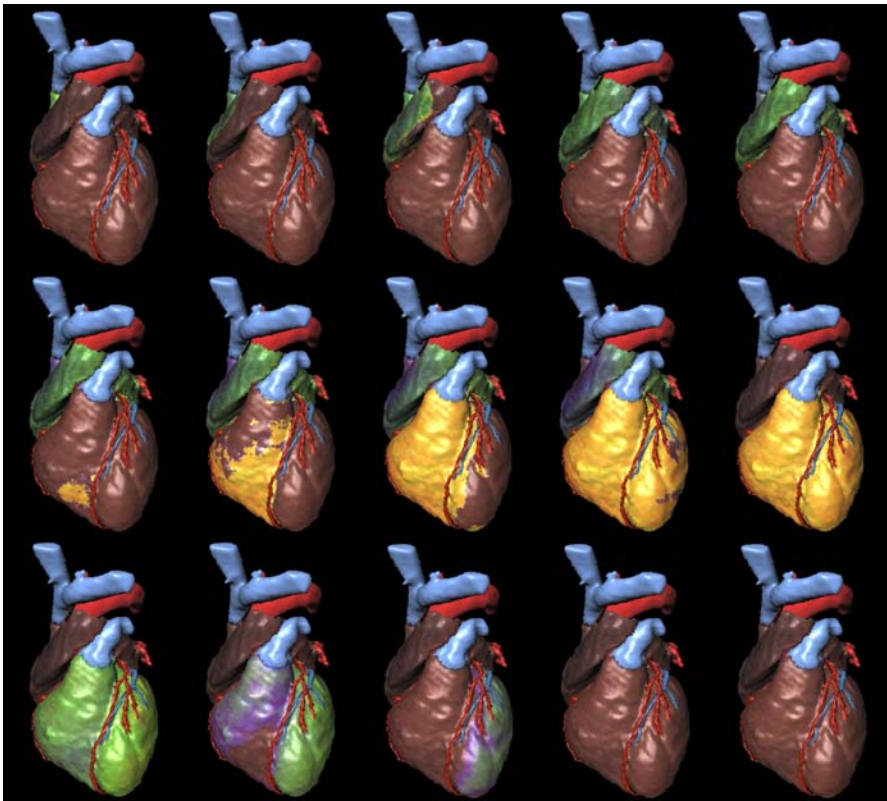


**Fig. 7.32.** Color coded transmembrane voltage distribution of subepicardial myocardium resulting from the simulation of a sinus rhythm (from [37]). The simulation is performed with a cellular automaton. Tissue specific variations of the maxima and duration of the transmembrane voltage are visible. Different time steps of the excitation process are visualized. The excitation starts in the sinus node located in the upper right atrium and propagates over the atrial myocardium. The atrioventricular node delays the propagation, which continues then spreading over the Tawara branches to the subendocardial Purkinje fibers. Finally, the excitation propagates over the ventricular myocardium.

The finite automaton at each node is configured with results from published measurements [23] and from simulations with electrophysiological cell models, e.g. simulations similar to those shown in Fig. 7.21. For that purpose, a large number of simulations was performed varying the cell model and the stimulus frequency. The simulations deliver tissue and stimulus frequency specific courses of the transmembrane voltage and of the excitation velocity.

The result of a simulation with the cellular automaton is the temporal and spatial distribution of the transmembrane voltage for each cell (Fig. 7.31, Fig. 7.32 and Fig. 7.33). This distribution can be used in subsequent numer-

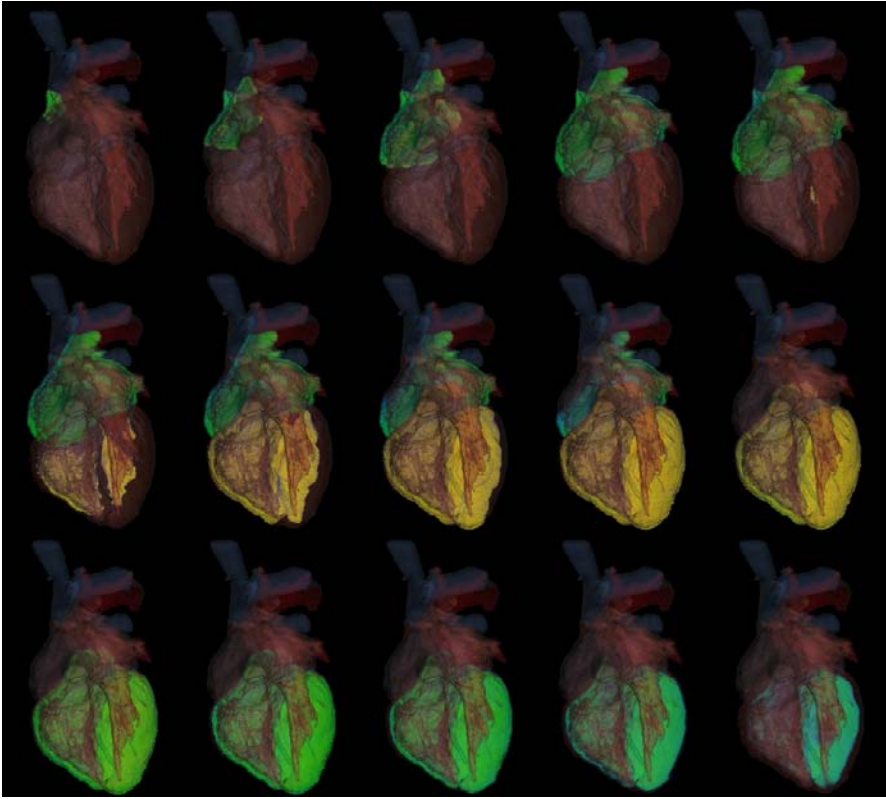


**Fig. 7.33.** Volume visualization of color coded transmembrane voltage distribution resulting from the simulation of a sinus rhythm (from [37]). The figure shows the same time steps as Fig. 7.32. The propagation through the volume of the heart, e.g. from the subendocardial located Purkinje fibers to the ventricular myocardium, is observable.

ical calculations of physical fields in the human body (Sect. 7.3.4), e.g. the calculation of the current source distribution in the heart (Fig. 7.34) and of the extracellular potentials in the whole body (Fig. 7.35). The potentials at the body surface can be used to determine electrocardiograms (Fig. 7.36). Hereby, for each time step the potentials at different points on the body surface are read out. The electrocardiograms of different type, e.g. Einthoven, Goldberger and Wilson leads, are calculated by their differences and averages.

*Simulation of unidirectional blocks, spiral and scroll waves.* A unidirectional block can be simulated with the cellular automaton for a suitably located and timed stimulus in the repolarization phase of the excitable media, e.g. atrial and ventricular myocardium [221, 224, 228, 232, 233]. In this case the excitation propagates in the direction opposite to the block. A stimulus is

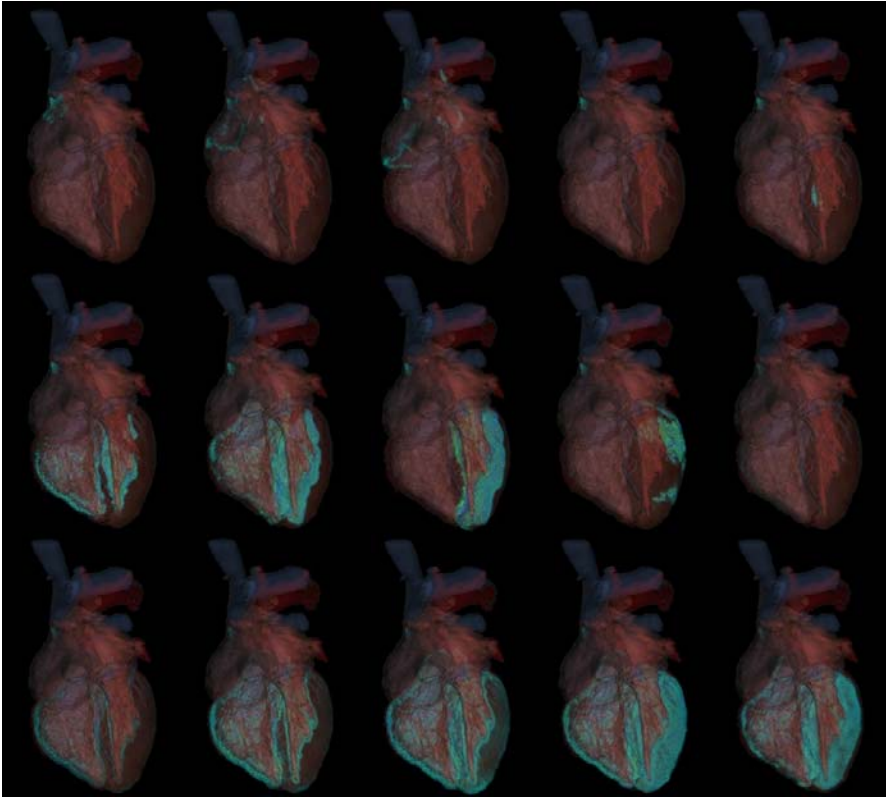


**Fig. 7.34.** Volume visualization of color coded current source density distribution of simulated sinus rhythm (from [37]). Different time steps of the excitation process are visualized. The sources are calculated with the bidomain model. They occur at places with a gradient of the transmembrane voltage, primarily at the front of the excitation propagation. No sources are found in the fully activated atrial and ventricular myocardium.

suitably located and timed, if it is located with one part in a non-excitabile area, with the other in an excitable area.

Depending on the dimension of the simulated area, different phenomena of excitable media resulting from a unidirectional block can be reconstructed in simulations with the cellular automaton. The reconstructability is depending on the specific implementation of the automaton.

While normally a stimulus in a one-dimensional domain is followed by two propagation fronts in each direction, a block leads to a propagation in the opposite direction. In an inhomogeneous two-dimensional domain a block can lead to a wave rotating around obstacles (Fig. 7.37). The block can produce single and multiple spiral waves, too. The spiral waves can rotate freely. No obstacles or specifically arranged geometrical structures are necessary. In sim-

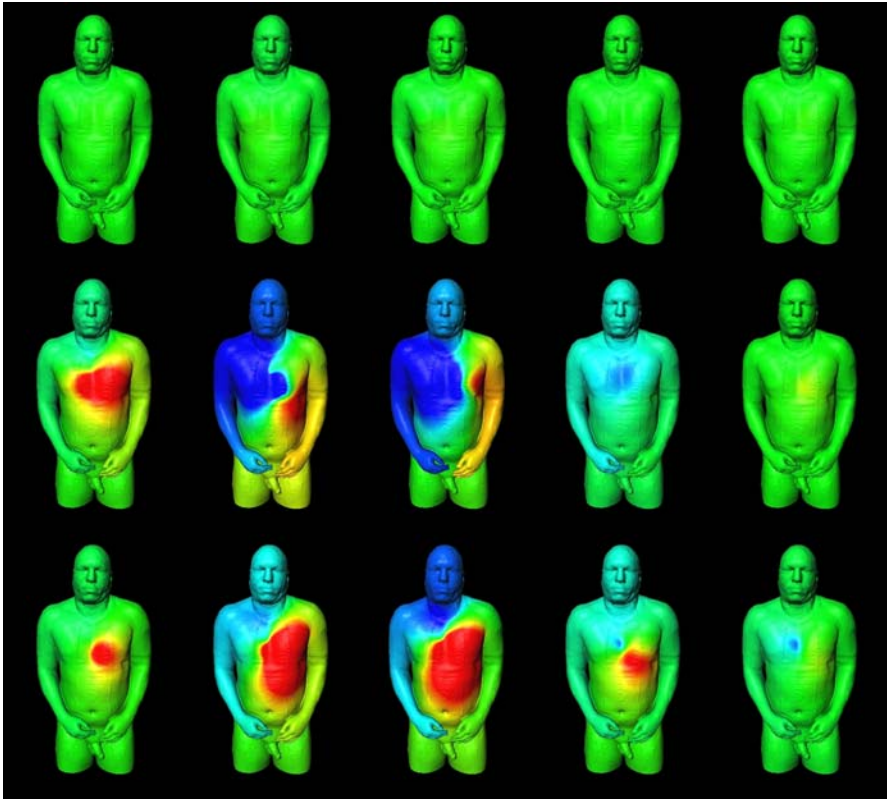


**Fig. 7.35.** Color coded body surface potential map of sinus rhythm (from [37]). Different time steps are visualized. The voltages at the body surface resulting from the cardiac sources are calculated with the finite difference method and a conductivity model of the whole body [26].

ulations with three-dimensional domains scroll waves can be reconstructed. The cellular automaton allows an efficient simulations in large and complex models, e.g. atrial and ventricular flutter can be simulated with models of the whole heart (Fig. 7.38 and Fig. 7.39).

*Simulated radiofrequency (RF) ablation in right human atrium.* A clinical option for the treatment of chronic atrial flutter is the catheter ablation therapy with radiofrequency current [234]. The applied current destroys cells in areas of the atrial myocardium, so that an excitation propagation through the area is suppressed. Commonly, lines of myocardium are ablated with end-points at the ostia of the atrium, e.g. to the vena cava superior and inferior. The location of the lines has to be chosen so, that a propagation from the sinus node to the atrioventricular node is still possible and the atrial flutter is permanently terminated.

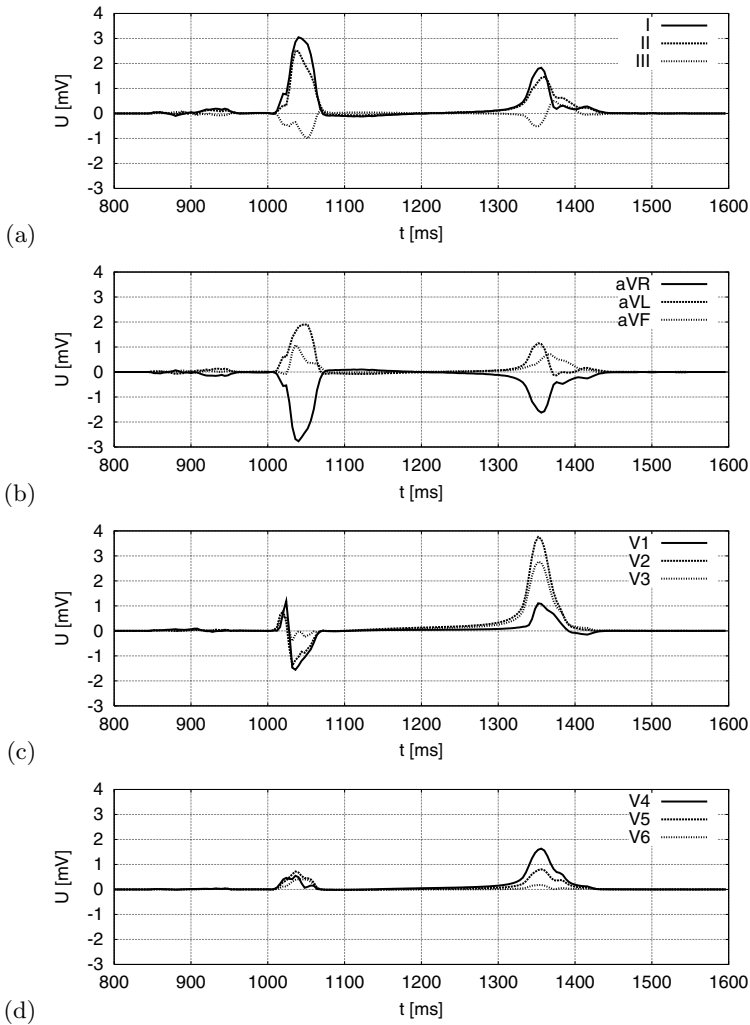


**Fig. 7.36.** Simulated electrocardiograms of sinus rhythm (from [37]). (a) Einthoven lead I, II and III, (b) Goldberger leads aVR, aVL and aVF, (c) Wilson leads V1, V2 and V3, (d) Wilson leads V4, V5 and V6.

The cellular automaton is capable of simulating the atrial flutter and the electrophysiological effects of an ablation therapy. In the exemplary simulation illustrated in Fig. 7.40 the atrial flutter is represented by a rotating wave around the vena cava inferior.

The rotation wave is terminated after execution of two ablation lines. A first line is set in the dorsal right atrial wall from the vena cava inferior to the vena cava superior. The first line results in a rotating wave around the



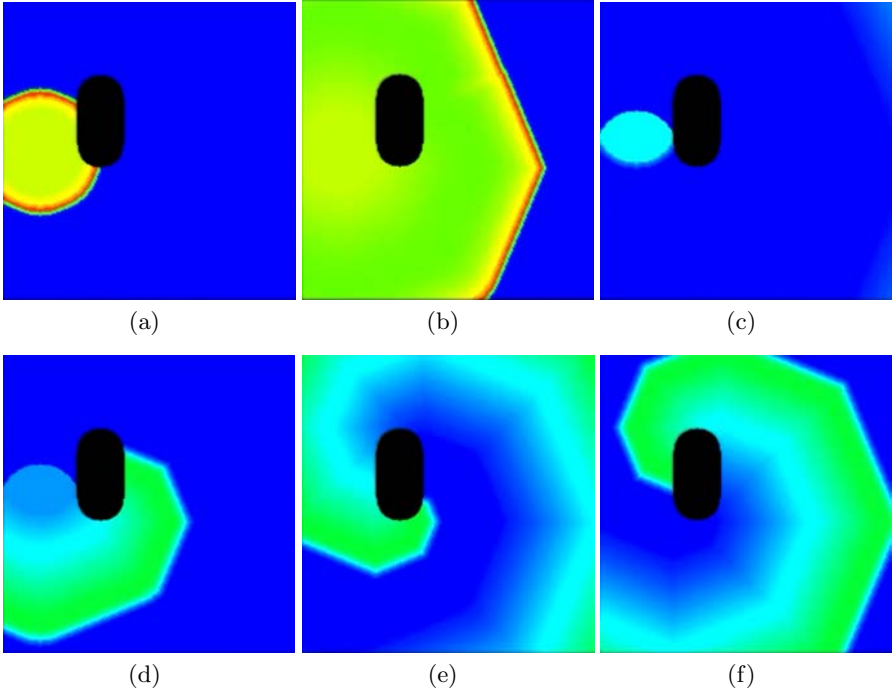


**Fig. 7.37.** Rotation of wave around an obstacle simulated with cellular automaton in a three-dimensional slice of  $256 \times 256 \times 3$  elements with a size of  $0.2 \text{ mm} \times 0.2 \text{ mm} \times 0.2 \text{ mm}$  modeling the electrophysiology of atrial cells. The simulated transmembrane voltage is color coded illustrated at different time steps. (a) A first stimulus was applied followed by (b) a wave propagating over the obstacle. (c) A second stimulus in the repolarization phase leads through a unidirectional block to an excitation propagation in the opposite direction. (d-f) The excitation propagates around the obstacle.

vena cava inferior and the ablation line, which leads to an increase of the cycle duration of the flutter. A second line is set orthogonal in the right area of the right atrium leading to a termination of the flutter. The ablation still permits the propagation from sinus node to the ventricles via the atrioventricular node, but a reinitiation of flutter with the same stimulus sequence is not possible.

#### 7.3.4 Reaction Diffusion Systems

**Overview.** Reaction diffusion systems, which are also known as excitable dynamics equations, use a system of non-linear partial differential equations to describe the excitation and propagation process in excitable media [235]. The system consists of  $n$  equations of the following type:

$$\frac{\partial u_i}{\partial t} = f_i(u_1, \dots, u_n) + \nabla \cdot (\mathbf{D}_i \nabla u_i) \quad i = 1, \dots, n$$

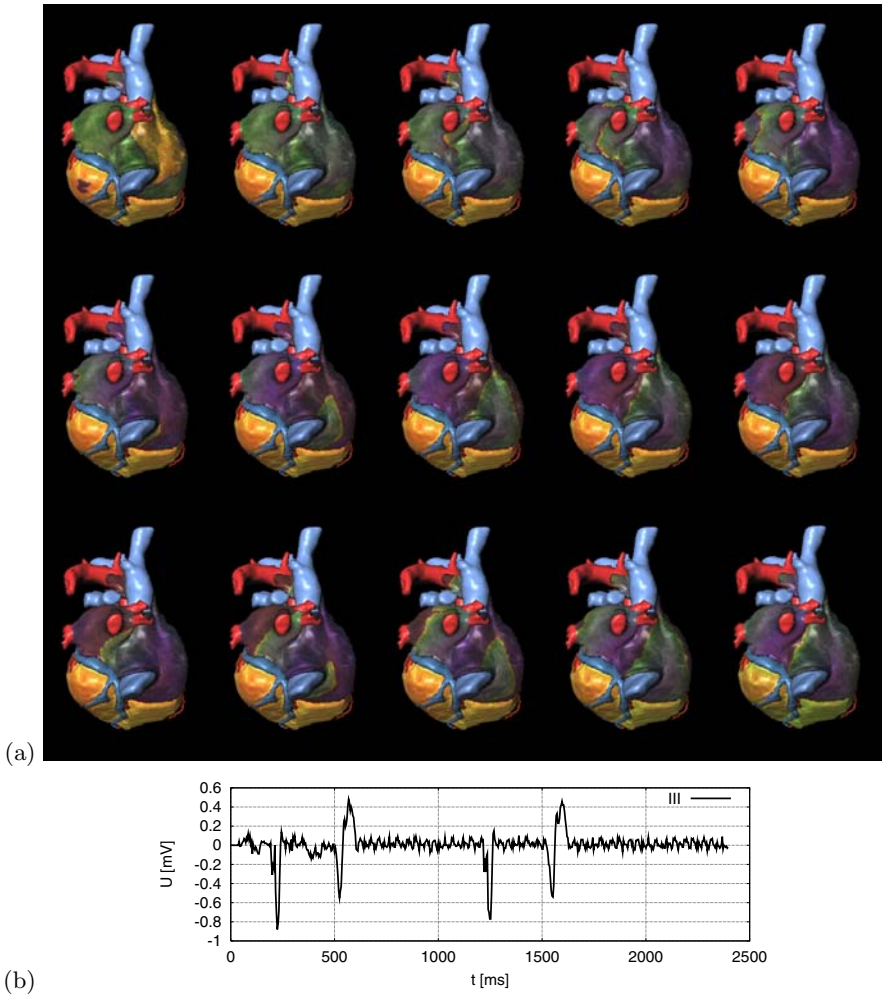


**Fig. 7.38.** Atrial flutter simulated with cellular automaton (from [37]). (a) A stimulus in the repolarization phase of the atrial myocytes leads through a unidirectional block to an excitation propagation in the opposite direction. The excitation propagates unidirectionally along the musculi pectinati. The reentry takes place at the dorsal right atrium near to the vena cava inferior. The excitation rotates around the ostium of the vena cava inferior. (b) The electrocardiogram shows a high frequency pattern for the atrial flutter in conjunction with normal QRS-complexes.

with the state variables  $u_i$ , the excitation term  $f_i$  and the diffusion tensor  $\mathbf{D}_i$ . In the context of cardiac excitation propagation, the state variables  $u_i$  correspond to the cellular status, e.g. transmembrane voltage, ionic channel



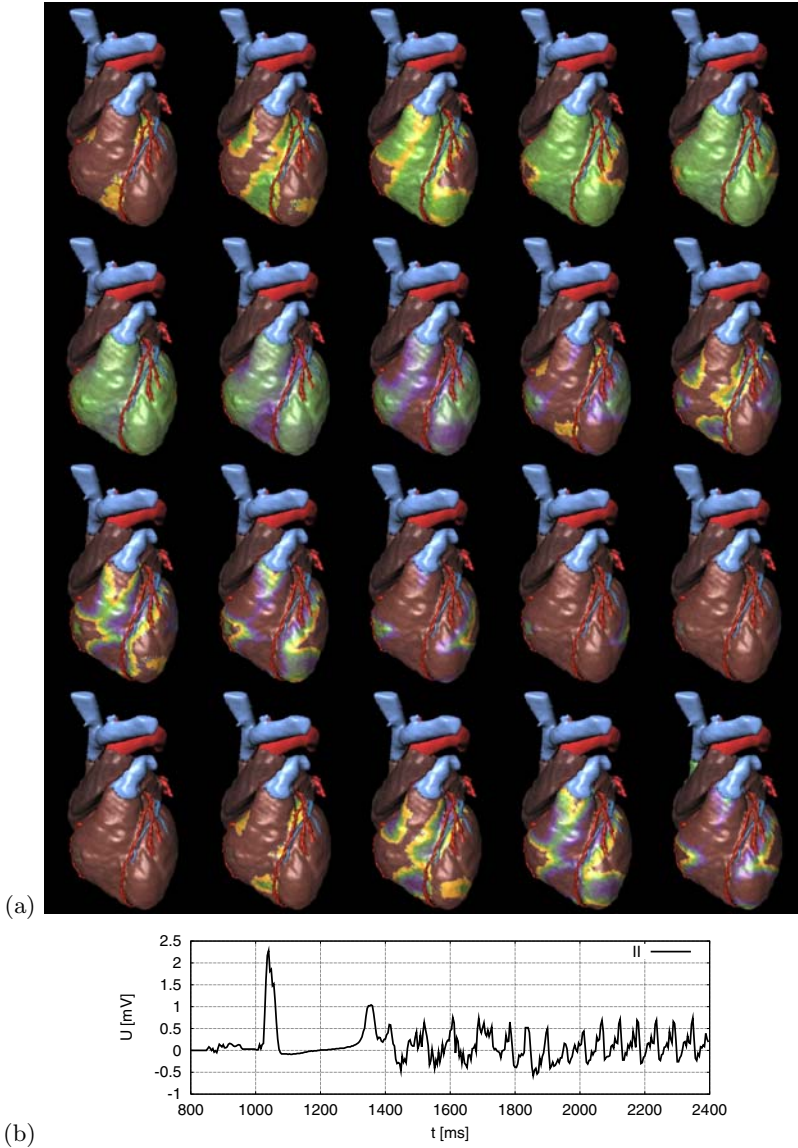


**Fig. 7.39.** Ventricular flutter simulated with cellular automaton (from [37]). (a) A stimulus in the repolarization phase of the left ventricular myocytes leads to a unidirectional block followed by ventricular flutter. (b) The electrocardiogram shows a high frequency pattern for the ventricular flutter.

conductivity and ionic concentrations. The change of the state variables is determined by the excitation term  $f_i$  and the diffusion term  $\nabla \cdot (\mathbf{D}_i \nabla u_i)$ .

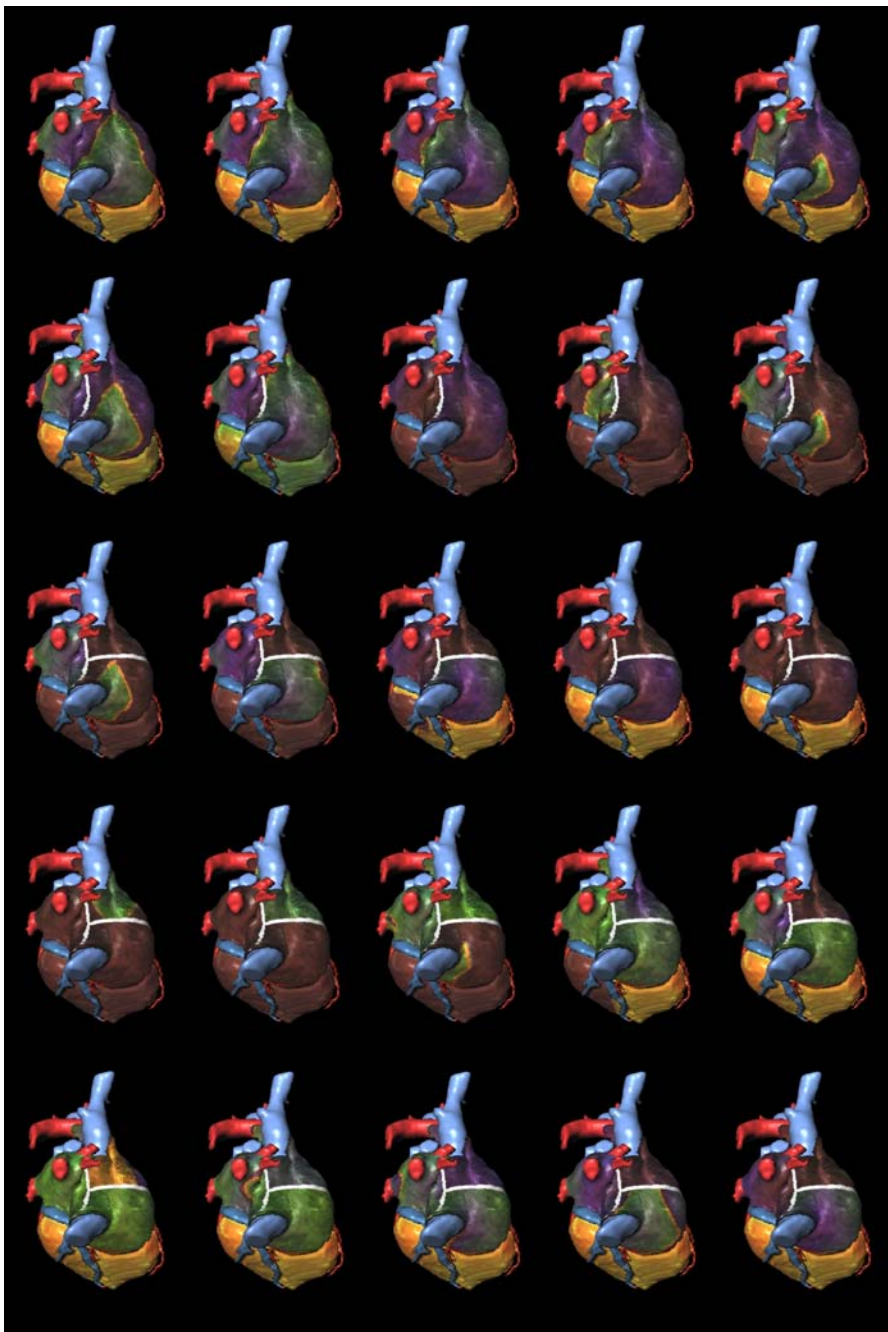


**Fig. 7.40.** Simulation of RF ablation in human right atrium with flutter (from [37]). The ablation lines are labeled in white.

Depending on the dimension  $n$  of the equation system as well as on the formulation of the excitation and diffusion terms different types of models can be distinguished:

- simplified approaches
- combinations of electrophysiological cell models with electrical current flow models
  - monodomain models with resistor networks or Poisson's equation
  - bidomain models with Poisson's equation

### Simplified Approaches

*Model of FitzHugh and Nagumo.* An early representation of the simplified approaches for excitation propagation is the two state FitzHugh-Nagumo model [236]:

$$\begin{aligned}\frac{\partial u}{\partial t} &= \frac{u - \frac{u^3}{3} - v}{\epsilon} + D\nabla^2 u \\ \frac{\partial v}{\partial t} &= \epsilon(u + \beta - \gamma v)\end{aligned}$$

with the state variable  $u$  for the transmembrane voltage and the state variable  $v$  for inhibition. The diffusion term is formulated for isotropic media with the scalar diffusion coefficient  $D$ . Typical parameters are  $0 < |\beta| < \sqrt{3}$ ,  $0 < \gamma < 1$  and  $\epsilon \ll 1$ .

*Model of Rogers and McCulloch.* A modification of the FitzHugh-Nagumo equations allows a more realistic description of the propagation in the myocardium [237, 238]:

$$\begin{aligned}\frac{\partial u}{\partial t} &= c_1 u(u - a)(1 - u) - c_2 uv + \nabla \cdot (\mathbf{D} \nabla u) \\ \frac{\partial v}{\partial t} &= b(u - dv)\end{aligned}$$

with the diffusion tensor  $\mathbf{D}$ , and the membrane parameters  $a$ ,  $b$ ,  $c_1$ ,  $c_2$ , and  $d$ . The additional parameters are used to reconstruct the course of the transmembrane voltage of ventricular myocytes. The state variables  $u$  and  $v$  describe as in the FitzHugh-Nagumo equations the transmembrane voltage and the inhibition. The boundary condition

$$\frac{\partial u}{\partial \mathbf{n}} = 0$$

is added, which allows to define the derivative of the transmembrane voltage at borders with normal  $\mathbf{n}$ . The equations were used in conjunction with finite element techniques to simulate the excitation propagation in two-dimensional sheets of myocardium.

Further adaptations of the FitzHugh-Nagumo equation in the area of cardiac electrophysiology are found in [239, 240, 241].

**Combinations of Electrophysiological Cell Models with Electrical Current Flow Models.** A biophysically well-founded approach consists of combining detailed electrophysiological models of single myocardial cells with models of the electrical current flow through the intra- and extracellular space as well as the gap junctions. The electrophysiological cell models describe the concentration and flow of ions as well as the conductivity of cellular structures and the transmembrane voltage by a set of coupled differential equations.

Two main representatives of these combined models were developed differing in the number of domains for the electrical current flow: mono- and bidomain models. The combined models are further distinguished depending on the representation of the conductivity used for the electrical current flow model. Hereby, approximations with isotropic and anisotropic conductivities represented by resistors as well as conductivity tensors of first or second rank are known.

*Monodomain Models.* The monodomain models incorporate the effect of coupled intracellular space with gap junctions by resistors [242, 243, 244] or conductivity tensors. In each time step and for each cell two calculations are performed:

- computation of the summary intracellular current source density  $f_i$  using a model of intercellular current flow
- updating of the status of the electrophysiological cell model using the current source densities  $f_{si}$

The summary intracellular current source density  $f_i$  can be calculated outgoing from Poisson's equation:

$$\nabla \cdot (\sigma_i \nabla V_m) = f_i \quad (7.2)$$

with the transmembrane voltage  $V_m$  and the intracellular conductivity tensor  $\sigma_i$ , describing conductivities for intracellular space and gap junctions. The summary intracellular current source density  $f_i$  consists of two different components:

$$f_i = \beta I_{tm} - f_{si} \quad (7.3)$$

with the intracellular current source density  $f_{si}$ , the transmembrane current  $I_{tm}$ , and the myocytes per volume ratio  $\beta$ , allowing the conversion from currents to current source densities. The current  $I_{tm}$  describes the summary flow through the membrane given by the electrophysiological model:

$$I_{tm} = C_m \frac{\partial V_m}{\partial t} + I_m \quad (7.4)$$

with the membrane capacitor  $C_m$  and the ionic current  $I_m$ , which is a function of the transmembrane voltage  $V_m$ . Additional stimulus currents are neglected. The inclusion of these definitions (equations 7.2-7.4) delivers the complete equation:

$$\nabla \cdot (\sigma_i \nabla V_m) = \beta \left( C_m \frac{\partial V_m}{\partial t} + I_m \right) - f_{si}$$

Numerically motivated the complete equation can be transformed to:

$$\frac{\partial V_m}{\partial t} = \frac{1}{C_m} \left( \frac{f_{si} + \nabla \cdot (\sigma_i \nabla V_m)}{\beta} - I_m \right)$$

The transformed equation is commonly solved with the finite-difference or finite-element method for the underlying generalized Poisson equation (Sect. 3.3) and the Euler or Runge-Kutta methods for the underlying ordinary differential equation (Sect. 2.5).

*Bidomain Models.* The bidomain models are an extension of monodomain models including the effects of the extracellular space [245, 246, 247, 248, 249]. The bidomain model treats the electrical behavior of tissue in two domains, in the intracellular and extracellular space, which are separated by the cell membrane. In each domain Poisson's equation for fields of stationary electrical current is fulfilled:

$$\begin{aligned} \nabla \cdot (\sigma_i \nabla \phi_i) &= \beta I_{tm} - f_{si} \\ \nabla \cdot (\sigma_e \nabla \phi_e) &= -\beta I_{tm} - f_{se} \end{aligned}$$

with the intracellular potential  $\phi_i$ , the extracellular potential  $\phi_e$ , the intracellular conductivity tensor  $\sigma_i$ , the extracellular conductivity tensor  $\sigma_e$ , the intracellular stimulus current source density  $f_{si}$ , the extracellular stimulus current source density  $f_{se}$ , and the myocyte per volume ratio  $\beta$ . The intracellular conductivity tensor  $\sigma_i$  consists of conductivities for the intracellular space and for the gap junctions. The domains are coupled by the summary current  $I_{tm}$  through the cell membrane and by the definition of the transmembrane voltage:

$$V_m = \phi_i - \phi_e$$

The summary membrane current  $I_{tm}$  vanishes in the summation of the two Poisson's equations:

$$\nabla \cdot (\sigma_i \nabla \phi_i) + \nabla \cdot (\sigma_e \nabla \phi_e) = -f_{si} - f_{se} \quad (7.5)$$

The following method can be chosen to couple the bidomain equations with the electrophysiological cell models (Fig. 7.41) [250]. The method uses a decomposition of the intracellular Poisson's equation:

$$\nabla \cdot (\sigma_i \nabla \phi_i) = \nabla \cdot (\sigma_i \nabla (V_m + \phi_e)) = \nabla \cdot (\sigma_i \nabla V_m) + \nabla \cdot (\sigma_i \nabla \phi_e)$$

and of the summation equation (equation 7.5):

$$\nabla \cdot (\sigma_i \nabla \phi_i) + \nabla \cdot (\sigma_e \nabla \phi_e) = \nabla \cdot (\sigma_i \nabla V_m) + \nabla \cdot ((\sigma_i + \sigma_e) \nabla \phi_e)$$

The method bases on the iterative solving of Poisson's equations with numerical techniques:

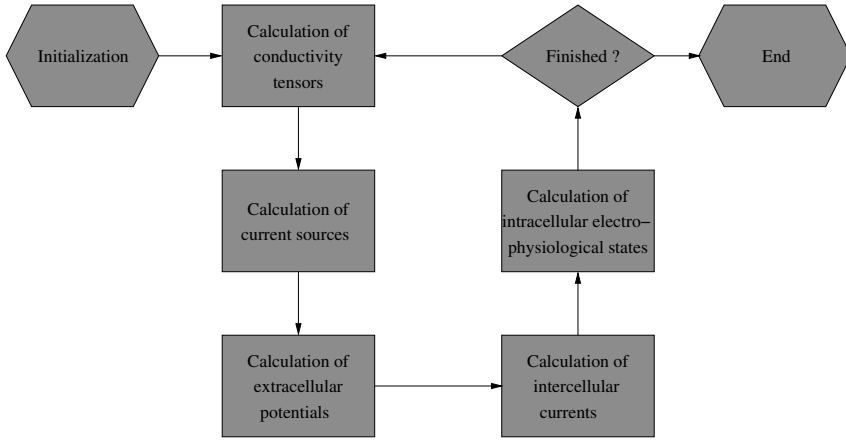


**Fig. 7.41.** Bidomain modeling of cardiac electrophysiology. The depicted modeling includes the possible adaption of conductivity, e.g. to incorporate deformation, which is neglected in traditional bidomain formulations.

- calculation of extracellular current sources  $f_e$  with the transmembrane voltage  $V_m$  delivered by the electrophysiological model
- computation of extracellular potentials  $\phi_e$  with the extracellular current source densities  $f_e$
- calculation of summary intracellular stimulus current source density  $f_i$  with the transmembrane voltage  $V_m$  and the extracellular potentials  $\phi_e$
- updating of the status of the electrophysiological cell model using the current source densities  $f_{si}$

The formulation neglects the extracellular stimulus current  $f_{se}$  for simplicity of description.

In a first step the extracellular current source density  $f_e$  delivered by the transmembrane voltage  $V_m$  is determined:

$$\nabla \cdot (\sigma_i \nabla V_m) = f_e$$

In a second step the extracellular potential  $\phi_e$  is calculated from the current source density  $f_e$ :

$$\nabla \cdot ((\sigma_i + \sigma_e) \nabla \phi_e) = -f_e$$

The calculation of  $\phi_e$  is commonly numerically expensive, because the solving of a large system of linear equations is necessary.

In a third step the summary intracellular current source density  $f_i$  is determined:

$$\nabla \cdot (\sigma_i \nabla V_m) + \nabla \cdot (\sigma_i \nabla \phi_e) = f_i$$

The incooperation of the electrophysiological model's equation (equation 7.4) and the separation of the intracellular current source density  $f_i$  (equation 7.3) lead to a combined equation:

$$\nabla \cdot (\sigma_i \nabla V_m) + \nabla \cdot (\sigma_i \nabla \phi_e) = \beta \left( C_m \frac{\partial V_m}{\partial t} + I_m \right) - f_{si}$$

with the membrane capacitor  $C_m$  and the ionic current  $I_m$  delivered by the electrophysiological model. The combined equation is numerically motivated transformed to:

$$\frac{\partial V_m}{\partial t} = \frac{1}{C_m} \left( \frac{f_{si} + \nabla \cdot (\sigma_i \nabla V_m) + \nabla \cdot (\sigma_i \nabla \phi_e)}{\beta} - I_m \right)$$

Commonly, the finite-difference or finite-element method is applied to solve the underlying generalized Poisson equations (Sect. 3.3). The Euler or Runge-Kutta methods is used to solve the underlying ordinary differential equation (Sect. 2.5).

*Simulations.* A set of simulations was performed to illustrate the excitation propagation model consisting of a combination of electrophysiological cell models with electrical current flow models. The simulations aim at the gain of knowledge, which is of importance for the construction of whole heart electro-mechanical models. Furthermore, they allow a comparison with cellular automata models.

As electrophysiological cell models served the Courtemanche-Ramirez-Nattel and Noble-Varghese-Kohl-Noble model [187, 189], which were solved with the Euler method. As current flow model the bidomain model was applied in conjunction with isotropic and anisotropic conductivities as well as with the finite-difference method to solve Poisson's equation. A time step of 0.025 ms was used for the repeated calculation of the electrophysiological and electrical current flow model.

*Two-Dimensional Simulations.* Spiral waves of different types were initiated in simulations with thin, plane slices approximating atrial myocardium. The slices consisted of 128 x 128 x 3 voxels with a size of 0.2 mm x 0.2 mm x 0.2 mm. Hereby, the bidomain model with isotropic extra- and intracellular conductivities was utilized in conjunction with the Courtemanche-Ramirez-Nattel model for atrial myocytes.

Stimulus sequences as described in Sect. 7.3.3 were used to create a unidirectional block with an excitation wave propagating in the opposite direction. The generation and evolution of freely rotating spiral waves are shown in Fig. 7.42. A wave rotating around an obstacle is illustrated in Fig. 7.43.

*Three-Dimensional Simulations.* In further simulations the physiologic and pathophysiologic excitation propagation in an area of the ventricular free wall was explored (Fig. 7.44). Hereby, an adapted Noble-Varghese-Kohl-Noble

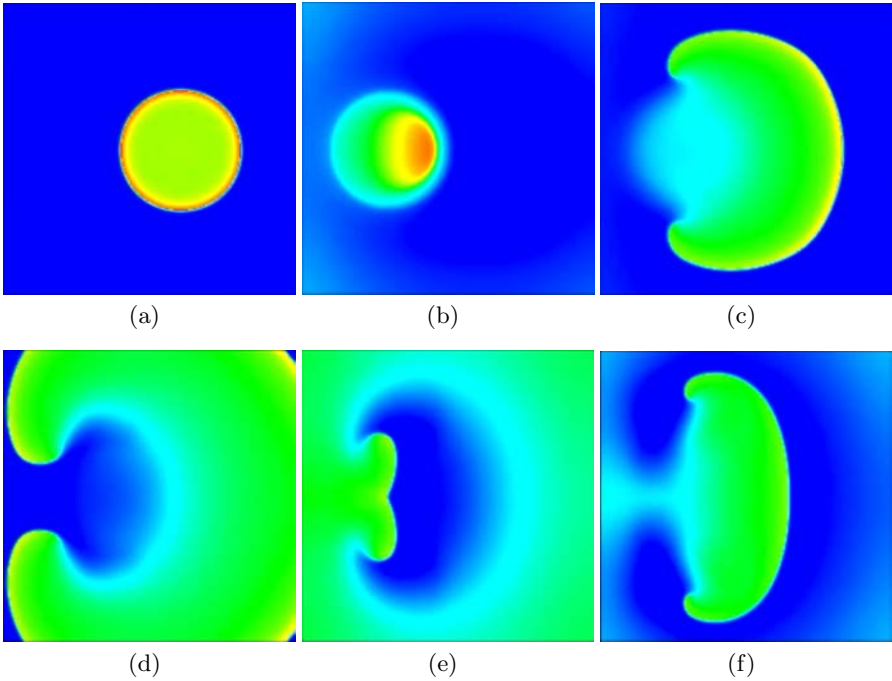


**Fig. 7.42.** Freely rotating spiral waves simulated with the bidomain model in a three-dimensional slice of  $128 \times 128 \times 3$  elements with a size of  $0.2 \text{ mm} \times 0.2 \text{ mm} \times 0.2 \text{ mm}$  modeling the electrophysiology of atrial cells. The simulated transmembrane voltage is color coded illustrated at different time steps. (a) A first stimulus was applied followed by a wave propagating over the whole area. (b) A second stimulus in the repolarization phase leads through a unidirectional block to an excitation propagation in the opposite direction. The timing and geometry of the stimulus create two mirrored rotors. (c-f) The two rotors generate spiral shaped wave fronts. The further behavior is primarily determined by the velocity of the excitation wave in the core of the rotors. Various effects were observed, e.g. meandering of the rotors as well as extinction, generation and detachment of wavelets.

model for ventricular myocytes was applied. The adaptation concerns the integration of a potassium current  $I_{to}$ , which was found to be dependent on the depth in the wall [160, 251, 252]. The bidomain model with anisotropic conductivities published in [248] was used. The area was described with  $150 \times 150 \times 125$  voxels, each with a size of  $0.2 \text{ mm} \times 0.2 \text{ mm} \times 0.2 \text{ mm}$ .

The myocyte orientation was incorporated varying from the subepicardial to the subendocardial myocardium. An angle of  $-70^\circ$  is assigned for the orientation at the ventricular subepicardial myocardium, an angle of  $70^\circ$  at the subendocardial myocardium [111][112]. The orientation in the space lying in between is interpolated outgoing from these boundary conditions by iterative averaging [64].



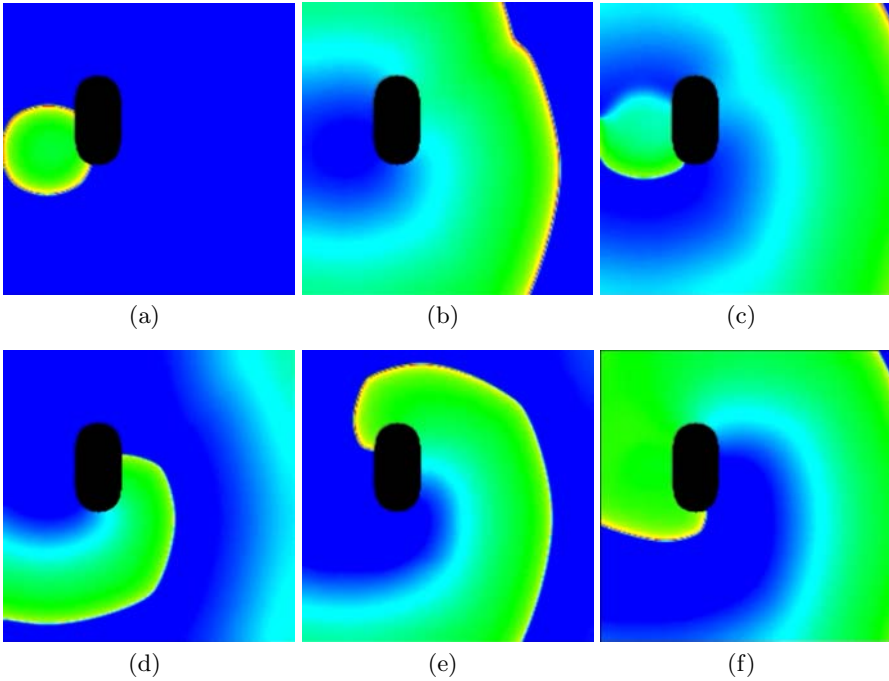


**Fig. 7.43.** Rotation of wave around an obstacle simulated with the bidomain model in a three-dimensional slice of  $128 \times 128 \times 3$  elements with a size of  $0.2 \text{ mm} \times 0.2 \text{ mm} \times 0.2 \text{ mm}$  modeling the electrophysiology of atrial cells. The obstacle consists of inactive cells with no intercellular coupling. The simulated transmembrane voltage is color coded illustrated at different time steps. (a) A first stimulus was applied followed by (b) a wave propagating over the obstacle. (c) A second stimulus in the repolarization phase leads through a unidirectional block to an excitation propagation in the opposite direction. (d-f) The excitation propagates around the obstacle. The further behavior is determined by the velocity of the excitation wave in relation to the geometry of the obstacle. An extinction as well as a detachment of the wave from the obstacle is possible.

The excitation of the heart wall is initiated at the subendocardial myocardium by applying pointwise a sufficiently large intracellular current. The points model location of myocytes with connections to Purkinje fibers. The applying of current starts at apical points and wanders in basal direction.

The physiologic excitation propagation in the ventricular free wall is visualized by evolution of the transmembrane voltage  $V_m$  (Fig. 7.45 (a) and Fig. 7.46). The propagation from the subendocardial to the subepicardial myocardium is reconstructed as well as the evolution of the repolarization. The evolution of the repolarization is found to be not similar to the depolarization. This behavior is observed in measurements. The differences are attributed to the variation of the potassium current  $I_{to}$ . Similar differences are found for the

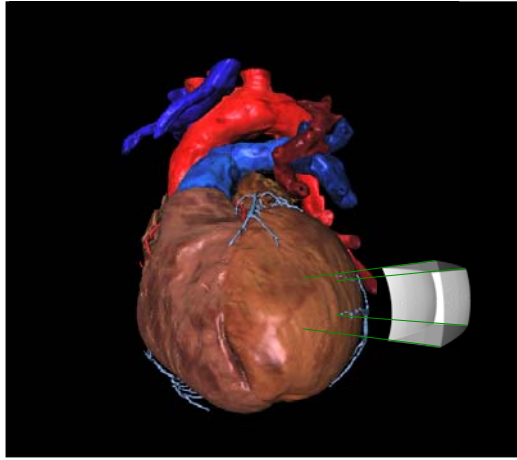


**Fig. 7.44.** Model of heart wall in anatomical context of whole heart. The model consists of  $150 \times 150 \times 125$  elements with a size of  $0.2 \text{ mm} \times 0.2 \text{ mm} \times 0.2 \text{ mm}$  modeling the electrophysiology of ventricular cells. The orientation of myocytes and the contribution of the ionic current  $I_{to}$  are varying in the cells from endocardium to epicardium. The cells are electrically coupled via the bidomain model using anisotropic conductivities.

evolution of the concentration of intracellular calcium  $[Ca^{2+}]_i$  (Fig. 7.45 (b) and Fig. 7.47). These differences lead to a non-homogeneity of the force development, which is not only depending on the process of excitation propagation, but also on the position in the heart wall.

A scroll wave is a representative of pathophysiologic excitation propagation (Fig. 7.48 (a)). The scroll wave is linked with significant changes of the concentration of intracellular calcium  $[Ca^{2+}]_i$  (Fig. 7.48 (b)).

### 7.3.5 Comparison of Macroscopic Models of Excitation Propagation

A comparison of traditional cellular automata and the reaction diffusion systems shows differences in the characteristics of the wave front and the reconstructability of cellular phenomena. These differences are observable in physiologic and pathophysiologic cases of the excitation propagation. Furthermore, significant distinctions are found concerning the demand of computing and main memory resources.

As characteristics of the wave front are considered its curvature and velocity. The wave front curvature of the reaction diffusion models is less obviously influenced by the neighborhood relationship of cells as of the traditional cellular automata [216]. An extreme case of influence can be found using the 6-neighborhood in cellular automata, which delivers rectangular propagation patterns. The velocity of the wave front is found to be dependent on

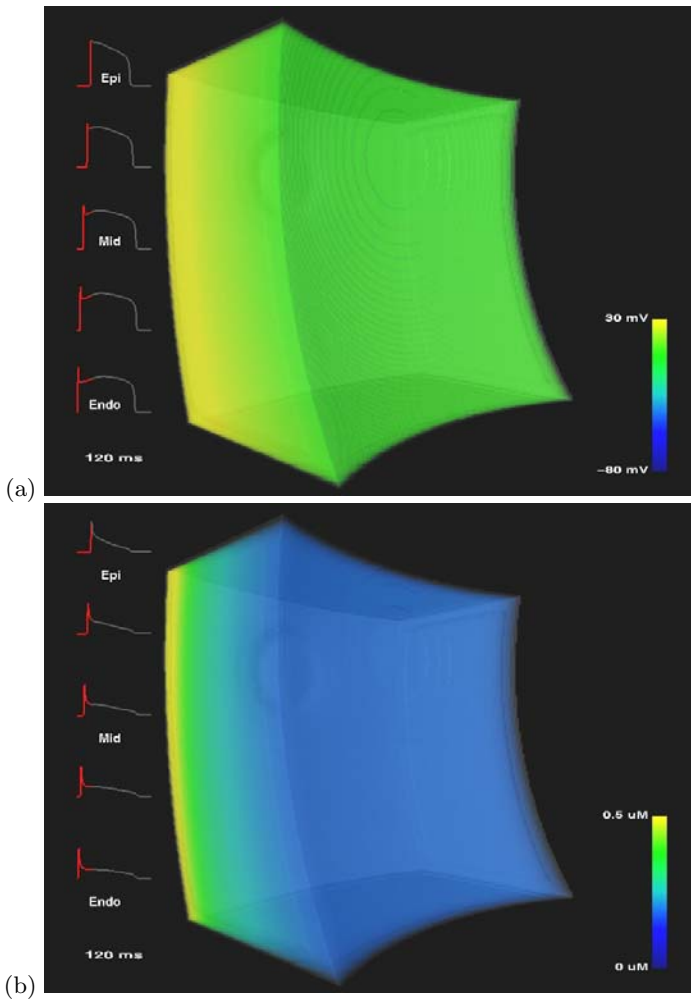


**Fig. 7.45.** Simulation of electrophysiology in static model of heart wall. (a) The transmembrane voltage  $V_m$  and (b) intracellular calcium concentration  $[Ca^{2+}]_i$  are visualized with volume based techniques at the exemplary point in time 120 ms. The corresponding color palette is located at the right side. At the left side the course of the transmembrane voltage  $V_m$  and the intracellular calcium concentration  $[Ca^{2+}]_i$  in different regions of the wall are illustrated.

its curvature in simulations with the reaction diffusion systems as well as in experiments with excitable media. Furthermore, the velocity varies with the stimulus frequency if the reaction term is suitably chosen. In contrast, the velocity is constant with traditional cellular automata. Whereas spirals and scroll waves generated with traditional cellular automata are stable and fixed, the phenomena are commonly instable in reaction diffusion systems caused

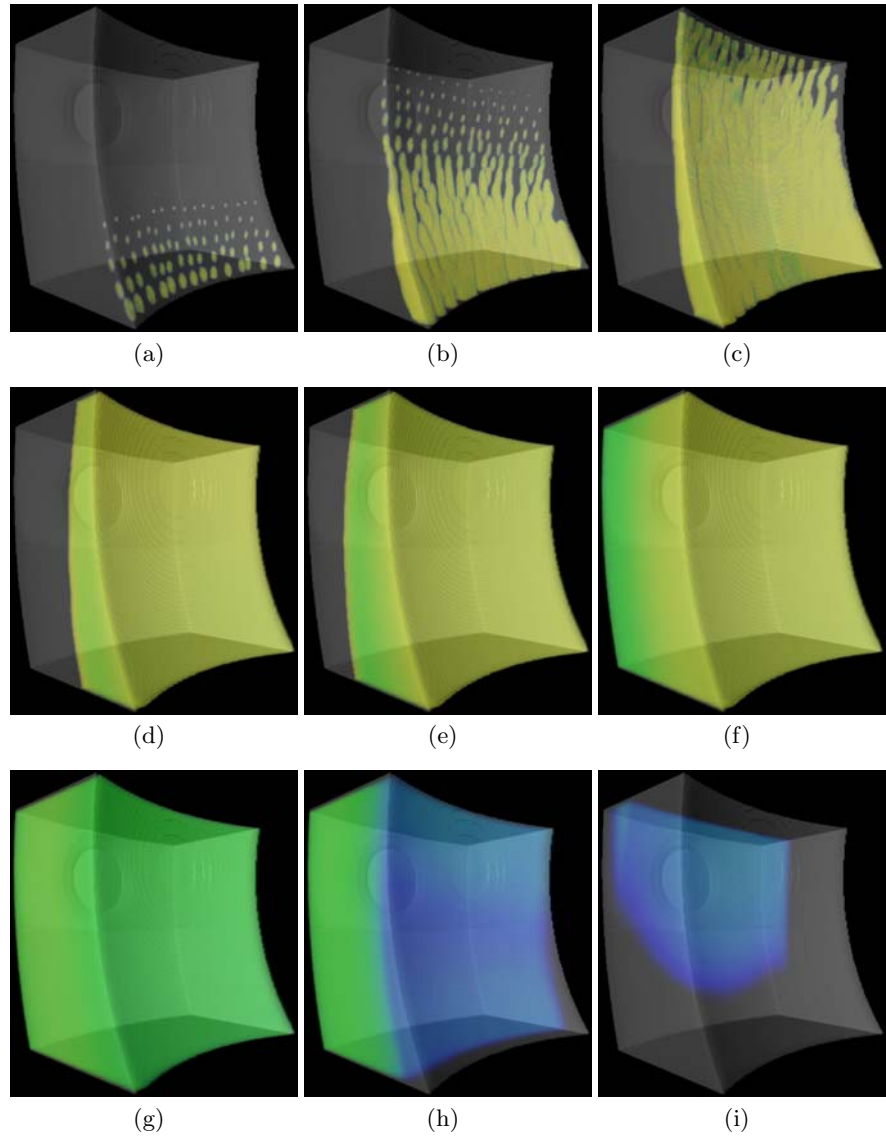


**Fig. 7.46.** Excitation propagation in static model of heart wall at different points in time. The simulated transmembrane voltage is visualized with volume based techniques at (a) 5 *ms*, (b) 10 *ms*, (c) 15 *ms*, (d) 30 *ms*, (e) 65 *ms*, (f) 130 *ms*, (g) 290 *ms*, (h) 340 *ms*, and (i) 410 *ms*.

by meandering, extinction and detachment of wavelets. These facts regarding the characteristics of the wave front apply for the simplified reaction diffusion systems as well as for the combined systems. Different approaches were chosen

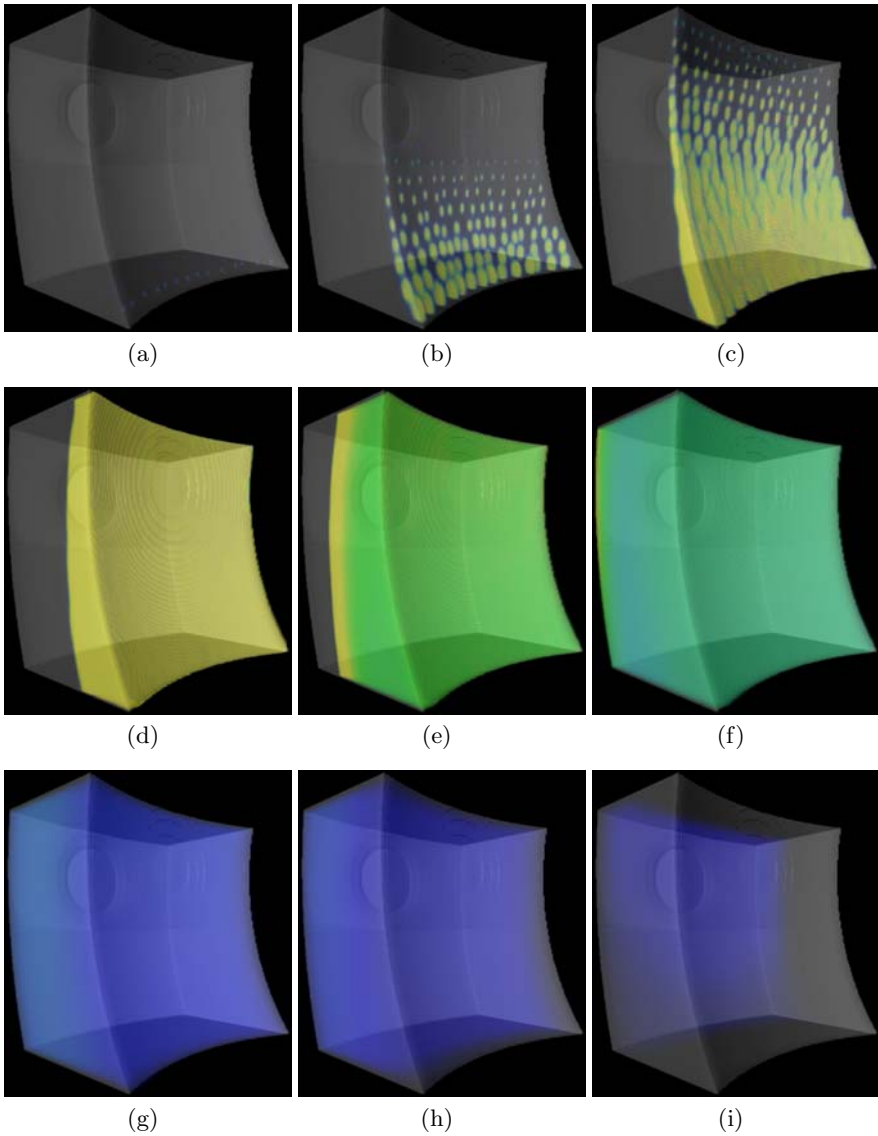


**Fig. 7.47.** Intracellular calcium concentration  $[Ca^{2+}]_i$  in static model of heart wall at different points in time. The simulated concentration is visualized with volume based techniques at (a) 5 ms, (b) 10 ms, (c) 15 ms, (d) 30 ms, (e) 65 ms, (f) 130 ms, (g) 290 ms, (h) 340 ms, and (i) 410 ms.

to approximate and reconstruct these characteristics with extended cellular automata.

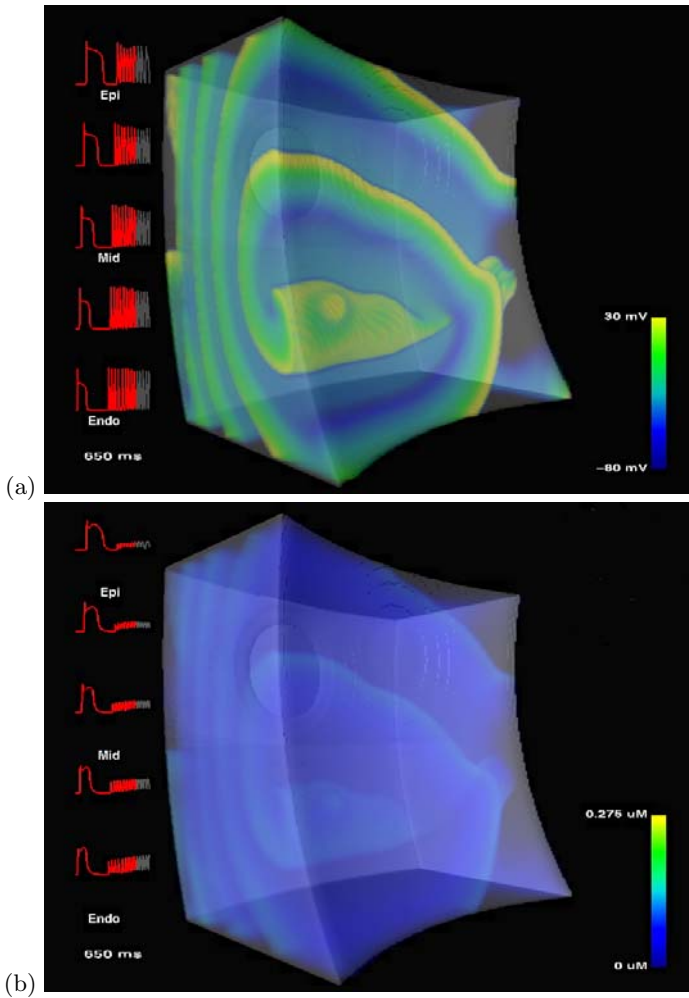


**Fig. 7.48.** Simulation of scroll wave in static model of heart wall. (a) The transmembrane voltage  $V_m$  and (b) intracellular calcium concentration  $[Ca^{2+}]_i$  are visualized with volume based techniques at the exemplary point in time 650 ms. The corresponding color palette is located at the right side. At the left side the course of the transmembrane voltage  $V_m$  and the intracellular calcium concentration  $[Ca^{2+}]_i$  in different regions of the wall are illustrated.

Cellular phenomena, e.g. EADs, DADs, and triggered activity, are commonly not reconstructed by cellular automata, although an inclusion is principally possible. The inclusion of complex cellular phenomena can be achieved by a modification of the finite automata working at each node of the cellular automaton.

The traditional cellular automata and the simplified reaction diffusion systems make the least demands on compute and storage resource. The demands of the combined models are primarily determined by the electrophysiological cell models and the numerical method to solve Poisson's equation. Nevertheless, these demands are strongly depending on the specific implementation and compute platform.